JOURNAL OF GEOPHYSICAL RESEARCH, VOL. 93, NO. B12, PAGES 15,016–15,036, DECEMBER 10, 1988

Active High-Resolution Seismic Tomography of Compressional Wave Velocity and Attenuation Structure at Medicine Lake Volcano, Northern California Cascade Range

JOHN R. EVANS

U.S. Geological Survey, Menlo Park, California

JOHN J. ZUCCA

Lawrence Livermore National Laboratory, Livermore, California

We determine compressional wave velocity and attenuation structures for the upper crust beneath Medicine Lake volcano in northeast California using a high-resolution active source seismic tomography method. Medicine Lake volcano is a basalt through rhyolite shield volcano of the Cascade Range, lying east of the range axis. The *Pg* wave from eight explosive sources which has traveled upward through the target volume to a dense array of 140 seismographs provides 1- to 2-km resolution in the upper 5 to 7 km of the crust beneath the volcano. The experiment tests the hypothesis that Cascade Range volcanoes of this type are underlain only by small silicic magma chambers. We image a low-velocity low-Q region not larger than a few tens of cubic kilometers in volume beneath the summit caldera, supporting the hypothesis. A shallower high-velocity high-density feature, previously known to be present, is imaged for the first time in full plan view; it is east-west elongate, paralleling a topographic lineament between Medicine Lake volcano and Mount Shasta. This lineament is interpreted to be the result of an old crustal weakness now affecting the emplacement of magma, both on direct ascent from the lower crust and mantle and in migration from the shallow silicic chamber to summit vents. Differences between this high-velocity feature and the equivalent feature at Newberry volcano, a volcano in central Oregon resembling Medicine Lake volcano, may partly explain the scarcity of surface hydrothermal features at Medicine Lake volcano. A major low-velocity low-Q feature beneath the southeast flank of the volcano, in an area with no Holocene vents, is interpreted as tephra, flows, and sediments from the volcano deeply ponded on the downthrown side of the Gillem fault, a normal fault mapped at the surface north of the volcano. A high-Q normal-velocity feature beneath the north rim of the summit caldera may be a small, possibly hot, subsolidus intrusion. A high-velocity low-Q region beneath the eastern caldera may be an area of boiling water between the magma chamber and the ponded east flank material. These structural data are useful both for understanding Cascade Range volcanism and for geothermal development in progress on the volcano.

INTRODUCTION

Medicine Lake volcano is a 600-km^3 shield volcano in the Cascade Range (Figures 1 and 2) [*Donnelly-Nolan*, 1988]. It lies 50 km ENE of Mount Shasta in northern California and has erupted a wide range of lava compositions, including Holocene rhyolites. Three lines of evidence led *Donnelly-Nolan* [1985] to conclude that Medicine Lake volcano may be a commercially viable geothermal prospect: the intermittent eruption of rhyolites for at least the last 1.25 m.y., evidence that the rhyolites erupted from high-temperature magma chambers, and evidence of fracture permeability at depth. More recently, *Donnelly-Nolan* [1986] emphasized the importance of repeated intrusion of basalt as a geothermal heat source at Medicine Lake volcano. Reports of steam venting from exploratory wells, and the high level of commercial interest in the volcano, support this conclusion.

Previous geophysical work has shown that Medicine Lake volcano is underlain by a shallow high-density high-velocity feature about 1 to 4 km beneath the caldera floor [*Finn and Williams*, 1982; *Zucca et al.*, 1986]. The deeper crust and upper mantle also may exhibit anomalously high velocities [*Evans*, 1982*a*]. The shallow feature has been interpreted as a plexus of subsolidus basalt to rhyolite composition intrusive rocks in the upper crystalline crust and lower Modoc Plateau volcanic rocks. The latter are about 2–3 km thick here. No low-velocity feature indicative of the presence of melt or partial melt, however, has been found at Medicine Lake volcano. Indeed, geophysical experiments have failed to produce convincing evidence of a magma chamber at any Cascade Range volcano. On the basis of this negative geophysical evidence and geological and geochemical evidence, the volcanic system is thought to consist of one or more small andesitic to rhyolitic magma chambers and many largely subsolidus basaltic dikes [*Donnelly-Nolan*, 1988, 1987; *Grove and Donnelly-Nolan*, 1986]. Small magma chambers, if present, may have escaped geophysical detection due to the limited resolution of the methods used.

This paper describes a high-resolution seismic tomography experiment performed to test this size hypothesis. This method was used first by *Hirn and Nercessian* [1980] and *Nercessian and Hirn* [1980]. A. Nercessian, A. Hirn and A. Tarantola authored the first journal article [*Nercessian et al.*, 1984]; consequently we call it the "NeHT" method (pronounced "Nat"). We use the NeHT method to resolve seismic velocity structures as small as 1 to 2 km across in a three-dimensional volume of the upper crust beneath the summit caldera and east flank of Medicine Lake volcano. *Stauber et al.* [1985] performed a similar experiment at Newberry volcano in central Oregon (Figure 1), and the results of that experiment are compared with ours

This paper is not subject to U.S. copyright. Published in 1988 by the American Geophysical Union.

Paper number 88JB03301.

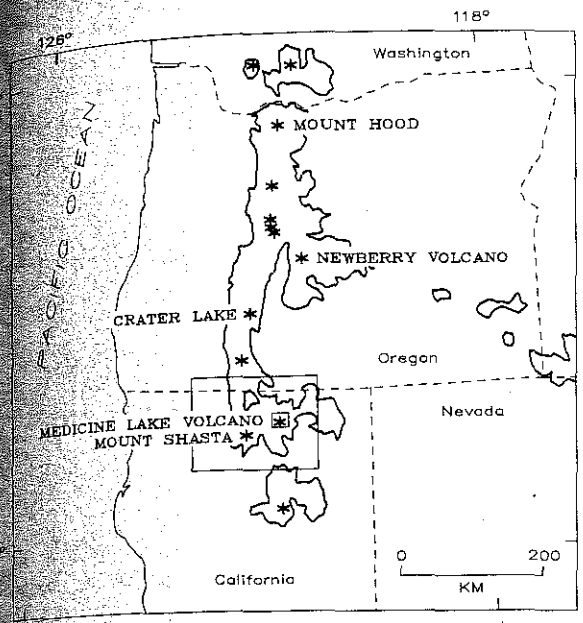

Fig. 1. Map of the southern Cascade Range showing location of Medicine Lake volcano, Newberry volcano and other Cascade Range volcanoes (stars). The larger box is the area of Figure 2; the smaller box is the area of Figure 3. Irregular areas are *King's* [1969] units Pe and Qv, described as "Youngest terrestrial volcanic rocks, mainly Quaterna-

own below. Finally, we present an extension of the NeHT method for imaging seismic attenuation structure using a δt^* method similar to the one described by *Young and Ward* [1981] and discuss the types of materials that can produce both the velocity and attenuation features observed.

GEOLOGIC SETTING

Medicine Lake volcano lies along a west striking topographic lineament connecting it with Mount Shasta (Figures 1 and 2) [*Donnelly-Nolan*, 1983, 1985; *Grove and Donnelly-Nolan*, 1986; *Anderson*, 1941]. It has produced a larger volume of extrusive rocks than Mount Shasta, the largest andesitic stratovolcano in the Cascade Range. Though of the same andesitic average composition as Mount Shasta, Medicine Lake volcano contains a broad suite of rocks ranging from primitive high-alumina (tholeiitic) basalts and andesites to dacites and rhyolites. Younger silicic lavas appear only in and around a 7×12 km summit caldera. By volume, mafic lavas greatly exceed silicic varieties, but small amounts of silicic lava have been extruded episodically through all or most of the volcano's ~1-m.y. history.

Medicine Lake volcano lies east of the Cascade Range axis in a back arc east-west extensional setting [*Donnelly-Nolan*, 1986]. It shares this easterly position, along with its shield form, compositional range, summit caldera, summit Holocene silicic eruptions, and Pleistocene to Holocene age range, with Newberry volcano, Oregon [*MacLeod et al.*, 1982] (Figure 1). Like Newberry volcano, Medicine Lake volcano overlies the westernmost north striking normal faults of basin-and-range type [*Donnelly-Nolan*, 1985] and exhibits vent alignments that are subparallel to and probably partly controlled by underlying normal faults. In particular, the vents of Glass Mountain, a late Holocene (~1100 years old) rhyolite and dacite volcano on the east rim of Medicine Lake caldera, strike NNW and are thought to be controlled by a southerly extension of the Gillem fault [*Donnelly-Nolan*, 1983]. The Gillem fault is an east-down normal fault (Figures 2 and 3).

Medicine Lake volcano differs from Newberry volcano, however, in having a physiographically less well-defined caldera. At Medicine Lake the summit depression simply is ringed by vents that have built a rampart of volcanoes around the depression, whereas Newberry has steep circular cliffs and well-mapped ring faults surrounding its summit caldera. Medicine Lake volcano also has fewer surface geothermal manifestations. Newberry volcano has several sets of hot springs in its caldera, which, though minor, greatly outnumber Medicine Lake

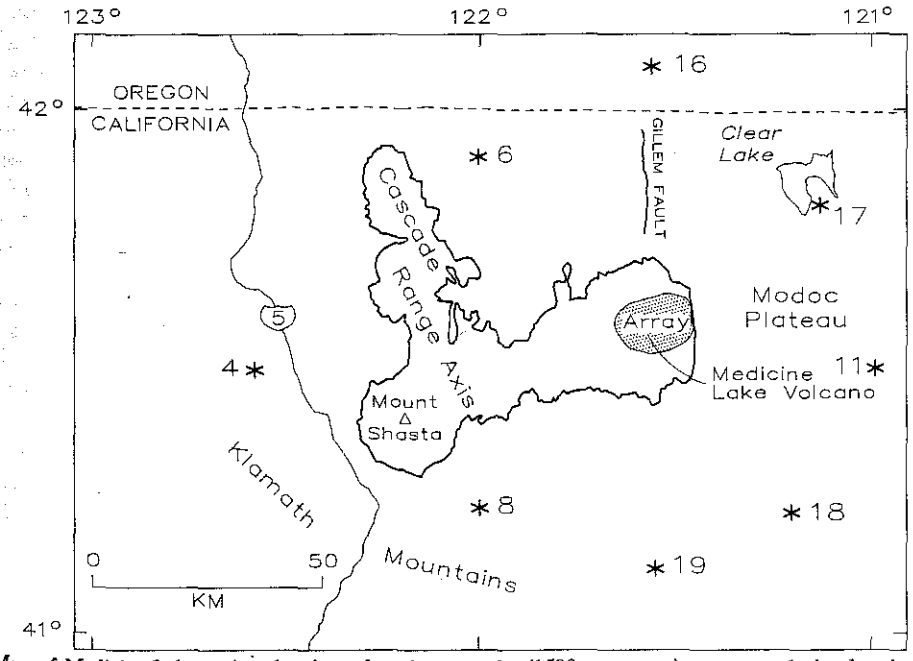

Fig. 2. Map of Medicine Lake region showing selected topography (1500-m contour), source explosion locations (numbered stars), and location of 140-seismograph array (stippled). See Figure 1 for the location of the map. Sources 4, 6, 8, and 11 are sited at the like-numbered sources of *Zucca et al.* [1986].

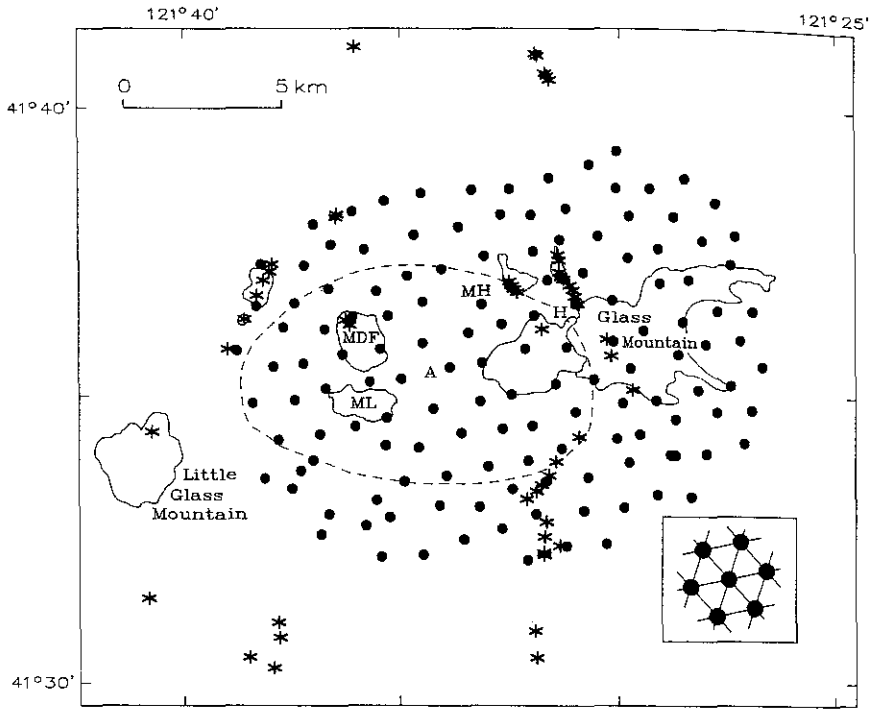

Fig. 3. Map of Medicine Lake volcano showing the caldera (dashed curve), Holocene silicic flows (solid curves), and Holocene vents (stars). The circles are the locations of seismographs used in this experiment. See Figure 1 for the location of the map. ML denotes Medicine Lake, MDF is the Medicine dacite flow of *Anderson* [1941], A is Arnica Sink, MH is Mount Hoffman (Hoffman flows are east and southeast of the MH symbol), and H is the "Hot Spot" fumarole. Geologic information is from J. Donnelly-Nolan (personal communication, 1985). The inset shows a portion of the idealized grid with seismographs at triangle vertices.

volcano's single fumarole, the "Hot Spot" (Figure 3). Thus caldera and hydrothermal expressions both appear to be greater at Newberry.

DESCRIPTION OF METHOD

We use the term "tomography" in the general sense, to mean any method in which a property's distribution within a volume is estimated from the integral of that property along each of many different paths through the volume. We do not follow the practice of some authors of implying that a particular inversion method is used. The volume in which this property is to be imaged is called the "target volume." In the case of seismic tomography, the property to be determined generally is seismic velocity or attenuation, and the line integral values are travel time or t^* along rays.

Ideally, one should have seismic sources and receivers at all points around the target volume. In practice, the number of sources and receivers available demands a sparser distribution. Also, the interaction between the velocity structure and the ray paths followed by seismic waves often makes the problem nonlinear.

Local earthquake tomography uses natural sources in the target volume and an array of seismographs at the surface [e.g., *Kissling et al.*, 1984]. Advantages of local earthquake tomography are the large number of sources often available, their depth distribution, and the short wavelength and consequent good resolving power of the phases used. The disadvantages include the problem's nonlinearity, due to the rays' sensitivity to velocity perturbations near their turning points, and the sometimes grossly uneven distribution of sources and seismographs. Uneven sampling of the target volume (in both ray density and incidence direction) can cause artifacts, such as the "smearing" of shallow low-velocity anomalies to beneath volcanic vents as discussed by *Achauer et al.* [1986]. The nonlinearity of the problem in areas lacking upward traveling rays from deep sources can lead to multiple solutions and thus to the need for extensive a priori information on the structure.

Teleseismic tomography uses distant earthquakes and a compact array of seismographs located above the target volume [e.g., *Iyer et al.*, 1981*a*, *b*]. Advantages of this method include the stability gained by using rays with no turning points in the target volume and the fairly even distribution of sources around the world which usually results in reasonably even sampling of the target volume. Disadvantages include the relatively poor resolution inherent in the ~1-Hz compressional phases used, difficulty in resolving horizontally oriented structures, and the loss of absolute velocity information that derives from a need to make assumptions about structure outside the target volume.

The NeHT method is intermediate between local earthquake tomography and teleseismic tomography. A ring of explosive sources is deployed around a small dense array of seismographs (Figure 2). The distance from the sources to the array is chosen to provide high-frequency upward traveling impulsive crustal phases in the target volume beneath the array (Figure 4). The resulting distribution of rays in the target volume is dense and even, limiting ray distribution artifacts. The lack of turning points in the target volume helps to linearize the problem, yet the high frequencies of crustal phases permit high-resolution imaging. However, structure outside the target volume must be removed from the problem, as described below, resulting in loss of absolute velocity or attenuation information.

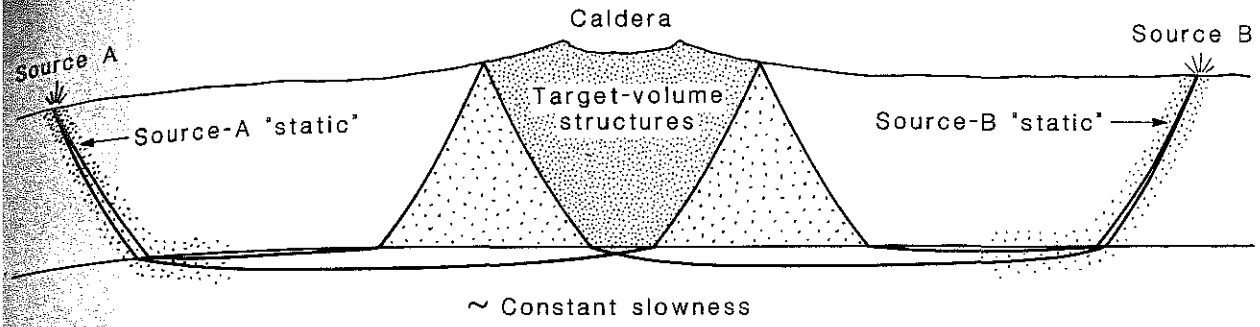

Fig. 4. Schematic of idealized structure modeled by least squares fit. The target volume is densely stippled. The light stippling next to target volume is partially resolvable. Light-stippled statics are regions modeled by intercept times (t_0) in the least squares travel time fit of Figure 6.

DESIGN OF EXPERIMENT

The summit caldera of Medicine Lake volcano and Glass Mountain on the caldera rim were selected as targets for a NeHT experiment to test the small magma chamber hypothesis. The caldera was selected because it is the focus of silicic activity, and Glass Mountain because it is the youngest silicic feature on the volcano. During the summer of 1985, the U.S. Geological Survey deployed 120 2-Hz vertical component seismographs and Lawrence Livermore National Laboratory deployed 16 2-Hz and four 1-Hz three-component seismographs in a 140-site 12×16 km oval array over these two features and surrounding areas (Figure 3). The array approximated a grid of packed equilateral triangles (Figure 3 inset) to give a more homogeneous distribution of rays than that provided by a rectilinear grid (i.e., we used "cubic closest packing"). Ideally, each seismograph has six equally distant nearest neighbors at the apices of a hexagon; the average distance to these nearest neighbors actually achieved was 1.27 km.

Eight 1360- to 1810-kg chemical explosive sources were deployed in a roughly circular pattern about 50 km from the seismograph array (Figure 2). Previous seismic refraction work by *Zucca et al.* [1986] indicates that the first-arriving phase at this distance usually is a coherent impulsive "*Pg*" wave with an apparent velocity of about 6.3 km/s and a turning point in the first or second velocity model unit with a velocity exceeding 6 km/s. Source 4 is farther from the array than the others and apparently produces a midcrustal reflected phase with an apparent velocity near 6.8 km/s [*Zucca et al.*, 1986, Figure 13]. No first-arriving, consistently available *PmP* or lower-crustal reflection was observed by Zucca et al., so none was used in this experiment.

The refraction models of northeastern California by *Zucca et al.* [1986] are based on five lines, each at least 100 km long. Their station spacing ranged from 0.5 to 1.75 km. Two of these lines passed across Medicine Lake volcano and are referenced repeatedly in this paper.

With these apparent velocities and the size of the seismograph array, it is possible to resolve structure to a depth of about 5 km beneath the array. The wavelengths of these phases in the center of the target volume range from about 0.6 to 1.1 km, so seismograph spacing, rather than wavelength, limits the resolution of this experiment to about 1¼ km. The number of available data reduces our effective resolution further, to about 2 km, as discussed in a later section. Seismograms, source and array coordinates, and related information are given by *Berge et al.* [1986].

COMPRESSIONAL WAVE VELOCITY STRUCTURE

In the first analysis, we measure travel times and invert these for compressional wave velocity structure in the target volume. With the NeHT method, absolute velocity information is lost when assumptions about structure outside the target volume are made. Thus we need not use first-arrival times. Instead, we use relative arrival times obtained from band-pass filtered seismograms by a correlative picking method (Figure 5) similar to that used for teleseisms [e.g., *Iyer et al.*, 1981*a*, *b*]. Since the same filter is used and the same feature (e.g., first trough in Figure 5) is timed on each trace of a given source, the delay between first arrivals and the picks is constant for the event, at least to the degree that the waveform is coherent up to that point. This constant is removed in the subsequent processing described below. This picking method also was employed in the Newberry volcano NeHT experiment by *Stauber et al.* [1985]. The repeatability of these picks is about ±0.01 s, substantially better than can be obtained for first arrivals (especially refracted ones) by conventional methods. Also, reliable picks can be obtained for many more seismograms than with first-arrival timing. We obtained 616 usable relative first-arrival times for use in imaging the structure of the target volume.

Calculating Travel Time Residuals

Isolating the effects of structure in the target volume from those of structures outside the volume is accomplished by converting travel times into travel time residuals. Two methods were compared.

First, we performed least squares first- and third-order polynomial fits to picked arrival times in Δ–t space, where the intercept time is allowed to be different for each source but higher-order terms of the polynomial are constant for all the sources. That is, for travel times plotted as a function of source-to-seismograph distance, we fit a series of parallel curves with constant shape and slope to the data. There is one curve, and hence one intercept time, for each source, but all higher-order coefficients describing the curve are constant for all eight sources. For a first-order (i.e., linear) fit of this type there is one slowness, but there are eight intercept times. Since geographic position is expressed only as Δ, the wave fronts are conical with a vertical axis passing through the source. Figure 6 shows the differences between best fitting and observed travel times, i.e. travel time residuals, for this linear fit. These are the primary data we used for the velocity imaging. We also performed a cubic polynomial fit of this type and observed almost no differences between it and the linear fit shown in Figure 6.

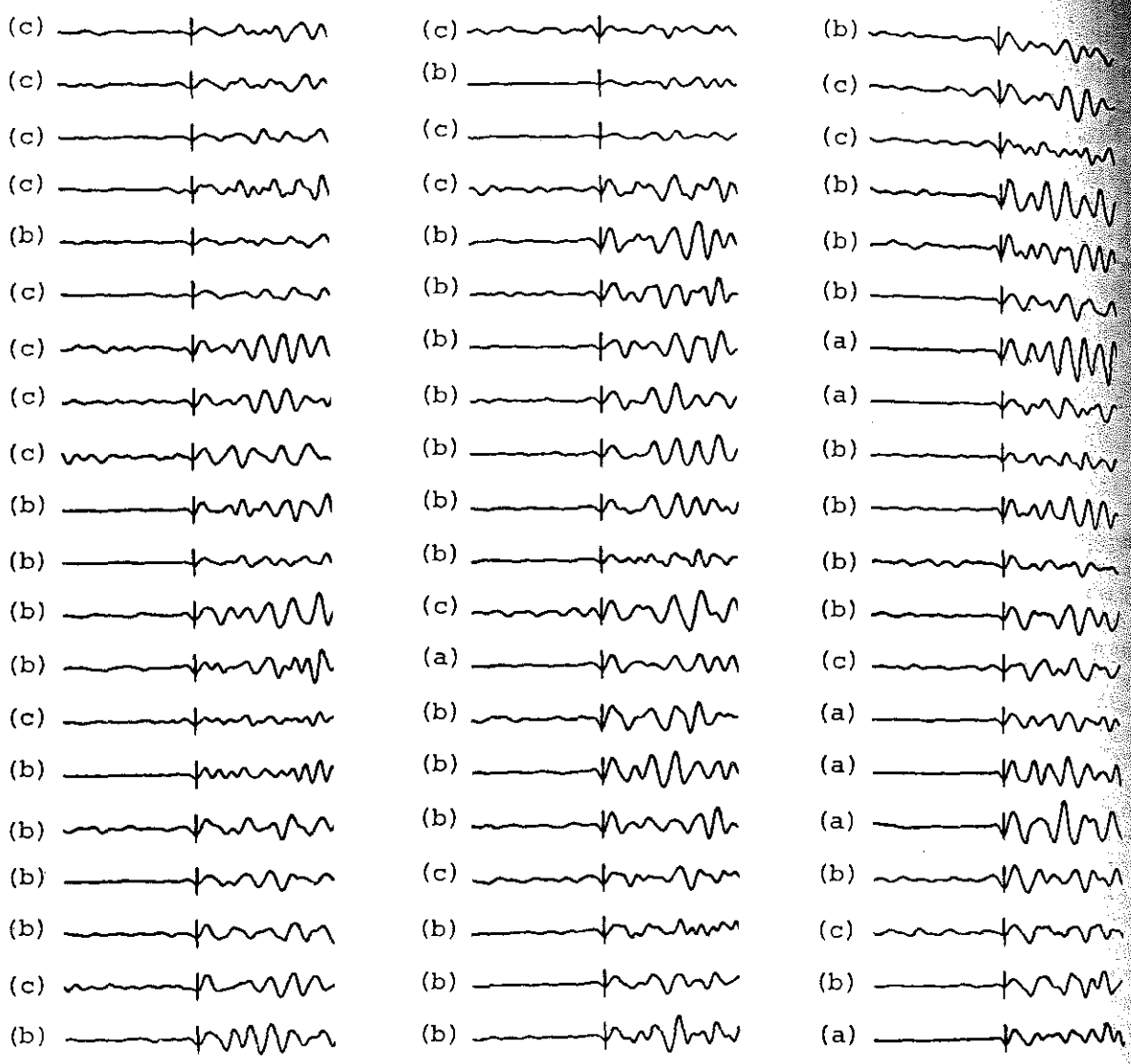

Fig. 5. Example of filtered correlative picks for an average quality source, number 17, from *Berge et al.* [1986]. Two seconds are shown of each trace; the filter band is 2.1–8.5 Hz; subjective quality is in parentheses (a is best, b is good, c is fair).

In effect, Figure 6 is a plot of travel time residuals where the Earth outside the target volume is assumed to have a velocity structure adequately modeled as in Figure 4. The intercept time acts as a "static" term to account for variations in structure near each source. Since these variations generally are greatest in the shallow sediments and weathered material directly beneath the source, where the ray bundle is most compact, modeling such a structure with a single travel time term for each source probably is adequate. In practice, both diffractive healing of the wave front and the tendency of the inversion discussed below to place the effects of structure outside the target volume into the periphery of the modeled volume mitigate any differences between the structure shown in Figure 4 and real Earth structure.

For comparison, we calculated travel time residuals by a second method. Apparent velocities derived from record sections and refraction models of *Zucca et al.* [1986] were assigned to the wave fronts a priori (6.3 km/s, except 6.8 km/s for source 4), and a static term was calculated for each source to provide zero-mean residuals, a least squares fit. Since only apparent velocities are different from Figure 6, the patterns are different from one another only by a linear gradient in Δ. Since this difference, in turn, has little effect on the important features of the data, no figure is included.

Except for source 4, these a priori apparent velocities are substantially lower than in the full least squares fit of Figure 6, which gives 6.95 km/s. Which velocities are appropriate is uncertain, but for reasons discussed next we prefer those of the full linear fit (Figure 6) over those of the a priori fit. This distinction is significant because it affects ray tracing in the inversion and because it causes residuals to be different by an amount depending on source-to-seismograph distance.

A deep core of high-velocity material which may be present beneath the volcano [*Evans*, 1982*a*] would increase the apparent velocity locally above the refracting-layer velocity. A similar midcrustal and upper crustal high-velocity anomaly was found by *Stauber et al.* [1988] beneath Newberry volcano. These observations, the volume dominance of mafic lavas, and the shallow depth of late-stage fractional crystallization to produce silicic lavas [*Grove and Donnelly-Nolan*, 1986] all suggest that the volcano is underlain by a plexus of basalt and pos-

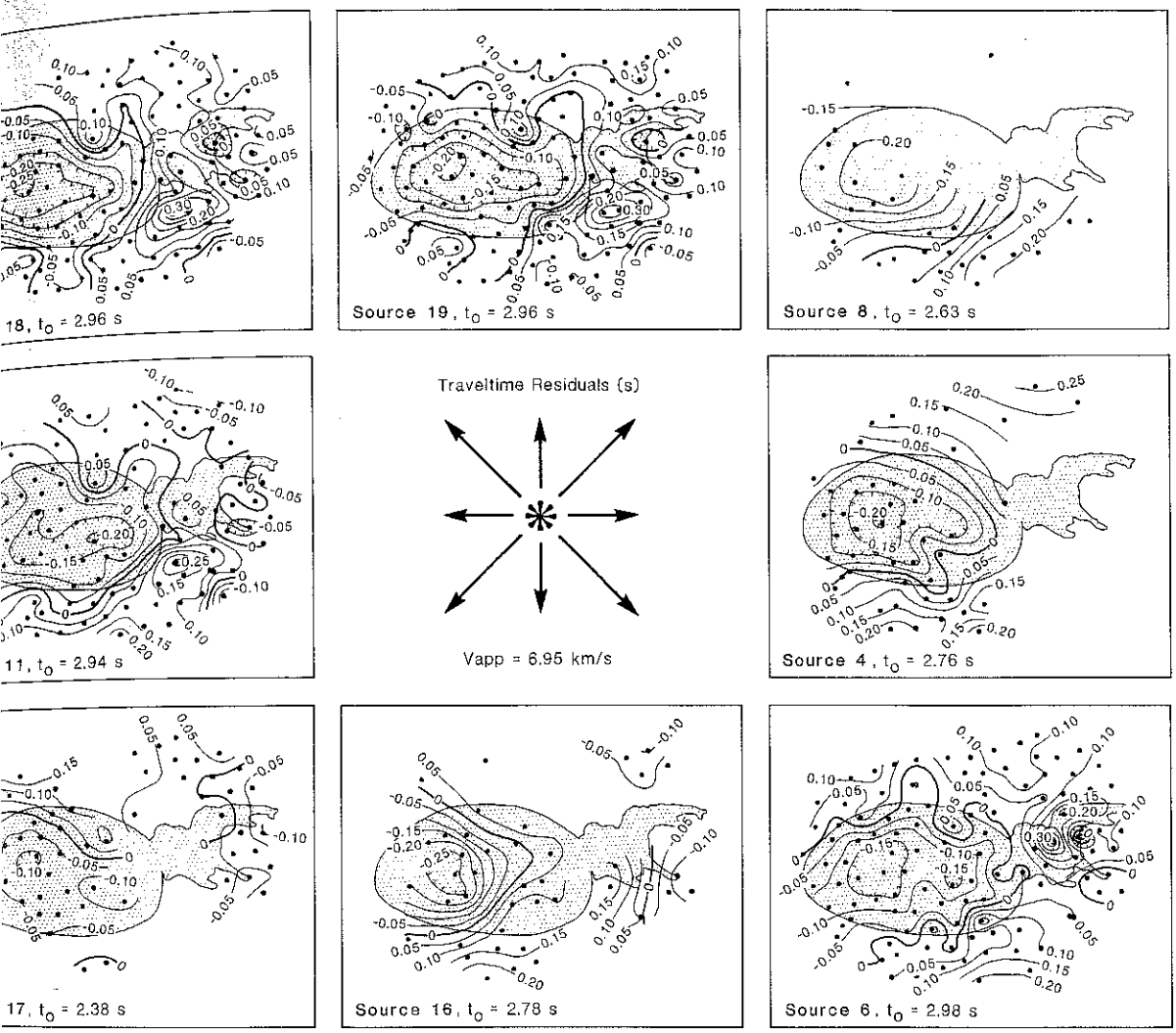

Fig. 6. Travel time residuals calculated by least squares linear fit with individual source static terms. The apparent velocity is 6.95 km/s; static terms (t_0) are given in the figure. The circles are where data exist; the contour interval is 0.05 s; the caldera and Glass Mountain are stippled. Contouring was done with commercial gridding and contouring routines; contours enclosing no data due to gridding overshoot have been deleted. The arrows in the center show the source-to-receiver azimuth for each plot. (The plots are arranged as if eight copies of the volcano were arrayed around a single source shown by the star.)

esite feeder structures reaching shallow depth. If so, pparent velocity of the full linear fit is reasonable. ttern of arrival times itself also suggests that there is imately radially systematic increase in apparent velocid the volcano. Indeed, time term analysis by W. ersonal communication, 1987) indicates that the vol- t the center of a radially symmetric pattern of early ome 30 km across. This pattern implies a local in apparent velocity of *Pg* to about 7 km/s on the to Medicine Lake volcano from any azimuth. In our 6.95-km/s best fitting apparent velocity also obviously a locally high average apparent velocity. Moreover, rity of the cubic and linear best fitting residuals indi- this increase is a long spatial wavelength feature. e five well-observed sources give apparent velocities of 46 km/s when fit independently by linear least squares, radial symmetry. (The three poorly observed sources pendently fit apparent velocities between 5.97 and 6.25 o produce this source independence, the increase in elocity must occur largely beneath the depth at which ndles from each source intersect one another. That is, it must occur largely outside the target volume, or it would carry the source-dependent short spatial wavelength signature of a resolvable structure. Thus it also is appropriate to use the higher apparent velocity in ray tracing for the inversions discussed below. Nevertheless, this uncertainty in the structure outside the target volume, expressed as uncertainty in apparent velocities, remains.

For either fitting method, note that any change in the absolute velocity of the whole target volume at any given depth produces a constant or nearly constant change in all measured arrival times. Since such changes are absorbed by the static source terms, information about absolute velocities in the target volume is lost. Thus travel time residuals calculated with static terms only contain information on velocity perturbations within the target volume. Thus the velocity models discussed below are given as percent variations rather than in kilometers per second.

Interpretation of Residuals

Qualitative interpretation of the residuals presented in Figure 6 is relatively straightforward. The ray bundle from each source

may be thought of as a slanted beam illuminating the structure from below and projecting shadows of the structure on the surface. Positive residuals are the shadows of low-velocity features; negative residuals are the shadows of high-velocity features. Since the residuals have zero mean, "high" and "low" are relative to the mean velocity of the target volume at any given depth, and the shadows of structures at different depths may overlap one another.

The plots for each shot are arranged in a ring at roughly their source-to-array azimuth. Thus the shadows of deeper features should consistently fall to the outside of the figure (as if there were one source of illumination at depth in the center of the figure and eight copies of the target volume and array surrounding it). Shallower anomalies produce shadows that move little, if at all, between different source azimuths.

The dominant feature of the travel time residual data is the region of early arrivals (negative residuals) centered in the western caldera and contrasting with a complex pattern of relatively delayed arrivals around the flanks of the volcano. This caldera high-velocity feature changes very little with source azimuth and thus is caused by a relatively shallow structure. It also changes very little with travel time fitting method and thus is not an artifact of data reduction. We believe that this caldera anomaly is the signature of the high-velocity high-density anomaly of *Zucca et al.* [1986] and *Finn and Williams* [1982]. Figure 6 is the first detailed seismic plan view mapping of this feature and shows it to be complex and asymmetrically disposed within the caldera. The asymmetry of the feature also is apparent in the east-west refraction line of Zucca et al. As discussed below, the vertical resolution of this feature using the NeHT method is not as good as that of the refraction experiment. Though the NeHT experiment indicates a shallow depth, we take the actual depth, about 1–3 km, from the refraction study. This depth is confirmed indirectly by the inversion analysis given below.

The pattern of residuals around the flanks of the volcano is complex and source-azimuth dependent. The major feature of this region is an area of delays (positive residuals) south of Glass Mountain. It is especially clear for sources 11, 18, and 19 but can be seen with source 8 as well. Its absence for source 6, one of the best sources in the experiment, indicates that the causal anomaly lies several kilometers deep. The other sources have no data where this anomaly is expected.

Though it is evident from Figure 6 that much of the east flank exhibits delayed arrivals, these delays are not as large as those south of Glass Mountain and are complicated by small areas of early arrivals near the east end of Glass Mountain and near the northeast corner of the array (e.g., source 11). In the inversion results discussed next, it becomes clear that both the southeast and northeast flanks of the volcano are anomalously slow but that the east flank beneath Glass Mountain is, by comparison, quite fast.

Inversion for Velocity Structure: Method

We inverted travel time residuals to obtain the compressional wave velocity structure in the target volume using a modified version of the "ACH" damped-least-squares method [*Aki et al.*, 1977]. The ACH inversion method is designed for the teleseismic tomography problem. Since the NeHT method has equivalent geometry, specifically no sources or turning points in the target volume, the ACH inversion is applicable. The inversion also is well understood by virtue of its use for over a decade by many investigators.

The modifications added here account for weighting the residuals by their estimated standard deviations and for variations in the seismograph-to-source azimuth, retaining the conical wave front of the travel-time-fitting methods. Earlier invocations of the ACH inversion assume a constant seismograph-to-source azimuth for each teleseism; however, the sources in this experiment are only about five array diameters away, and azimuths vary significantly across the array.

Following the derivation of *Ellsworth* [1977], the ACH inversion relies on a linearization of the travel time integral to the form

$$\delta t = -\int_{\text{ray}} \frac{1}{v_0}\frac{\delta v}{v_0} ds \tag{1}$$

where δt is the travel time perturbation caused by velocity variation δv about a starting model v_0 and ds is distance along the ray path. Refraction due to δv is disregarded, and ray tracing is only through v_0. We introduce parameterization of the medium by dividing it into blocks assigned the dimensionless quantity

$$\delta m_k = -\frac{\delta v}{v_0}\delta_k \tag{2a}$$

where δ_k is a Dirac delta equal to one inside block k and zero elsewhere. In block k, δm_k is approximately a slowness perturbation. Thus (1) becomes

$$\frac{\delta t}{\delta m_k} = -\int_{\text{ray}} \frac{1}{v_0^2}\frac{\delta v}{\delta m_k} ds \tag{2b}$$

where $\delta v/\delta m_k$ is understood to be zero outside block k. For block, source, and seismograph indices, we use the capital letter to indicate the maximum of the index. Thus there are K blocks, and for a given source $j=1, \cdots, J$ and seismograph $i=1, \cdots, I_j$, the travel time residual is

$$r_{ij} = dO_j + \sum_{k=1}^{K}\left\{-\int_{\text{base}}^{\text{seismograph } i} \frac{1}{v_0^2}\frac{\delta v}{\delta m_k} ds\right\}\delta m_k + e_{ij} \tag{3}$$

where e_{ij} is an error term, and the integral now is from the horizontal base of the model volume because the slowness has been removed from r_{ij} by the least squares fitting discussed above. The source term dO_j is introduced because absolute velocity and other unresolvable static terms may be present in the data. The part inside braces is called a_{ijk}. Because $\delta v/\delta m_k$ is zero outside block k and equal to the local value of $-v_0$ inside the block, a_{ijk} is the unperturbed travel time of ray ij inside block k.

Extending *Ellsworth's* [1977] derivation, we introduce weighting by the estimated error of r_{ij}, called σ_{ij}. These weights are normalized by the mean of such estimated errors, $\bar{\sigma}$, to preserve the physical significance of the damping term θ^2 introduced below in (9). Dropping the error term so that the equality now is approximate, (3) becomes

$$\frac{\bar{\sigma}}{\sigma_{ij}} r_{ij} = \sum_k \frac{\bar{\sigma}}{\sigma_{ij}} a_{ijk}\delta m_k + \frac{\bar{\sigma}}{\sigma_{ij}} dO_j \tag{4}$$

Premultiplied by $\frac{\bar{\sigma}}{\sigma_{ij}}[a_{ij1}, \cdots, a_{ijK}, 1]^T$, summed over i, and expanded, (4) becomes

$$\begin{bmatrix} w_{ij}a_{ij1}a_{ij1} & \cdots & w_{ij}a_{ij1}a_{ijK} & w_{ij}a_{ij1} \\ \cdot & & \cdot & \cdot \\ \cdot & & \cdot & \cdot \\ \cdot & & \cdot & \cdot \\ w_{ij}a_{ijK}a_{ij1} & \cdots & w_{ij}a_{ijK}a_{ijK} & w_{ij}a_{ijK} \\ w_{ij}a_{ij1} & \cdots & w_{ij}a_{ijK} & w_{ij} \end{bmatrix} \begin{bmatrix} \delta m_1 \\ \cdot \\ \cdot \\ \cdot \\ \delta m_K \\ dO_j \end{bmatrix} \quad (5)$$

σ^2/σ_{ij}^2. The summation limit I_j depends on j since a different number of data generally are available source.

ing the dummy block index l and $\overline{r}_j=\sum w_{ij}r_{ij}$, $_{ijk}$, and $\overline{w}_j=\sum w_{ij}$ (where the summations are from the last equation in (5) yields

$$dO_j = \frac{\overline{r}_j}{\overline{w}_j} - \sum_{l=1}^{K} \frac{\overline{a}_{jl}}{\overline{w}_j} \delta m_l \quad (6)$$

g (6) in the kth equation of (5) gives

$$\sum_{i=1}^{I_j} \left[r_{ij} - \frac{\overline{r}_j}{\overline{w}_j} \right] = \sum_{i=1}^{I_j} \sum_{l=1}^{K} \left[w_{ij} \left[a_{ijk}a_{ijl} - \frac{\overline{a}_{jk}\overline{a}_{jl}}{\overline{w}_j^2} \right] \right] \delta m_l \quad (7)$$

over J sources and noting that the sum over l is a ltiplication gives

$$\mathbf{G}m=b \quad (8)$$

$=[\delta m_1, \cdots, \delta m_K]^T$. The kth element of b is the left- of (7) in brackets, and the k-lth element of $\mathbf{G}$ is the part in brackets, each summed over i and j. Equa- solved by damped least squares, as in the usual ACH

$$\hat{m} = (\mathbf{G}+\theta^2\mathbf{I})^{-1}b \quad (9)$$

n show that $\mathbf{G}$ and b may be written in terms of d (a $N_{obs}=\sum I_j$ observed residuals, r_{ij}), $\mathbf{A}$ (the $N_{obs}\times K$ a_{ijk} terms), and $(\mathbf{W}-\mathbf{P})$ (a weighting and parameter matrix). Thus

$$\hat{m} = (\mathbf{A}^T(\mathbf{W}-\mathbf{P})\mathbf{A} + \theta^2\mathbf{I})^{-1}\mathbf{A}^T(\mathbf{W}-\mathbf{P})d \quad (10)$$

is a diagonal matrix of w_{ij} weights and $\mathbf{P}$ is the block matrix with jth block

$$\mathbf{P}_j = \frac{1}{\overline{w}_j} \begin{bmatrix} w_{1j}w_{1j} & \cdots & w_{1j}w_{I_jj} \\ \cdot & & \cdot \\ \cdot & & \cdot \\ \cdot & & \cdot \\ w_{I_jj}w_{1j} & \cdots & w_{I_jj}w_{I_jj} \end{bmatrix} \quad (11)$$

(10) is equivalent to the familiar form of (9) usually the literature and is the solution of

$$\mathbf{A}m=d \quad (12)$$

with weighting and with parameter separation for the dO_j term given by (6).

In estimating the variance σ_r^2 remaining after the inversion, the usual development is by analogy with standard least squares [*Draper and Smith*, 1966]:

$$\sigma_r^2 = \frac{e^Te}{N_{free}} = \frac{(d-\mathbf{A}m)^T\mathbf{W}(d-\mathbf{A}m)}{N_{obs} - (N_{blocks} + N_{sources})} \quad (13)$$

where the denominator is the number of degrees of freedom (number of observations N_{obs} minus the number of parameters estimated, one per block for the δm_k values and one per source for the dO_j values). For the numerator, this development [e.g., *Achauer et al.*, 1986] gives

$$d^T\mathbf{W}d - \hat{m}^T\mathbf{A}^T\mathbf{W}d - \hat{m}^T\theta^2\hat{m} \quad (14)$$

which is used in this paper. Note, however, that the least squares analogy is faulty because the damped-least-squares inverse is not an unbiased estimator (i.e., $E(e)\neq 0$) (M. Mathews, personal communication, 1987). However, *Ellsworth* [1977] compared the unweighted equivalent of (14) to results of ray-tracing tests and found it to be reasonable in complex models, though it underestimated the ray-tracing result by about 5%.

Inversion for Velocity Structure: Results

Inversion results for the best fitting residuals of Figure 6 are shown in Figures 7 and 8. They require explanation and interpretation. Artifacts are present and we use several techniques to deal with them and to extract maximum information from the data. It is tempting but dangerous to *think* of tomographic models as pictures of the Earth. They are, in reality, transforms of the data and require thoughtful analysis to avoid pitfalls. At the end of this section, these models also will be compared to inversions of the a priori residuals described above.

Figure 7 shows the four layers of the inversion model derived from the data in Figure 6. These data were weighted using the subjectively assigned arrival time pick qualities of *Berge et al.* [1986]. Normalized inverses of estimated standard errors (0.01 s for quality "a," 0.02 s for "b," and 0.05 s for "c") were used. We call Figure 7 the "direct" inversion result.

The first complication is that a smoothing algorithm has been applied to Figure 7. The actual inversions performed used the block sizes, layer thicknesses, and initial velocities listed in Table 1 and shown in Figure 9. With this initial model, a ratio of about 1.4 is maintained between observations and unknowns. However, the output of an ACH inversion tends to model the noise fraction of the data as a high spatial frequency oscillation (because the damping minimizes squared model length, $|\hat{m}|^2$, rather than maximizing model smoothness). Also, artifacts can be introduced by the arbitrary positioning of block boundaries [*Ellsworth*, 1977]. Therefore, to reduce the noise oscillations, obviate block boundary effects, and maximize the spatial resolution of the inversions, each inversion shown actually is a spatial average of the results of nine separate, horizontally offset ACH inversions. In each of these nine models, each layer except the first is offset horizontally by one of the nine permutations of zero-, $\frac{1}{3}$-, and $\frac{2}{3}$-block offsets along the directions of the block edges. Each block used in layers 2 to 4 of Figures 7 and 8 is one third the dimensions of the blocks in the offset models and represents the overlap region of one block from each of the nine offset models. As a result, the averaging kernel shown in Fig-

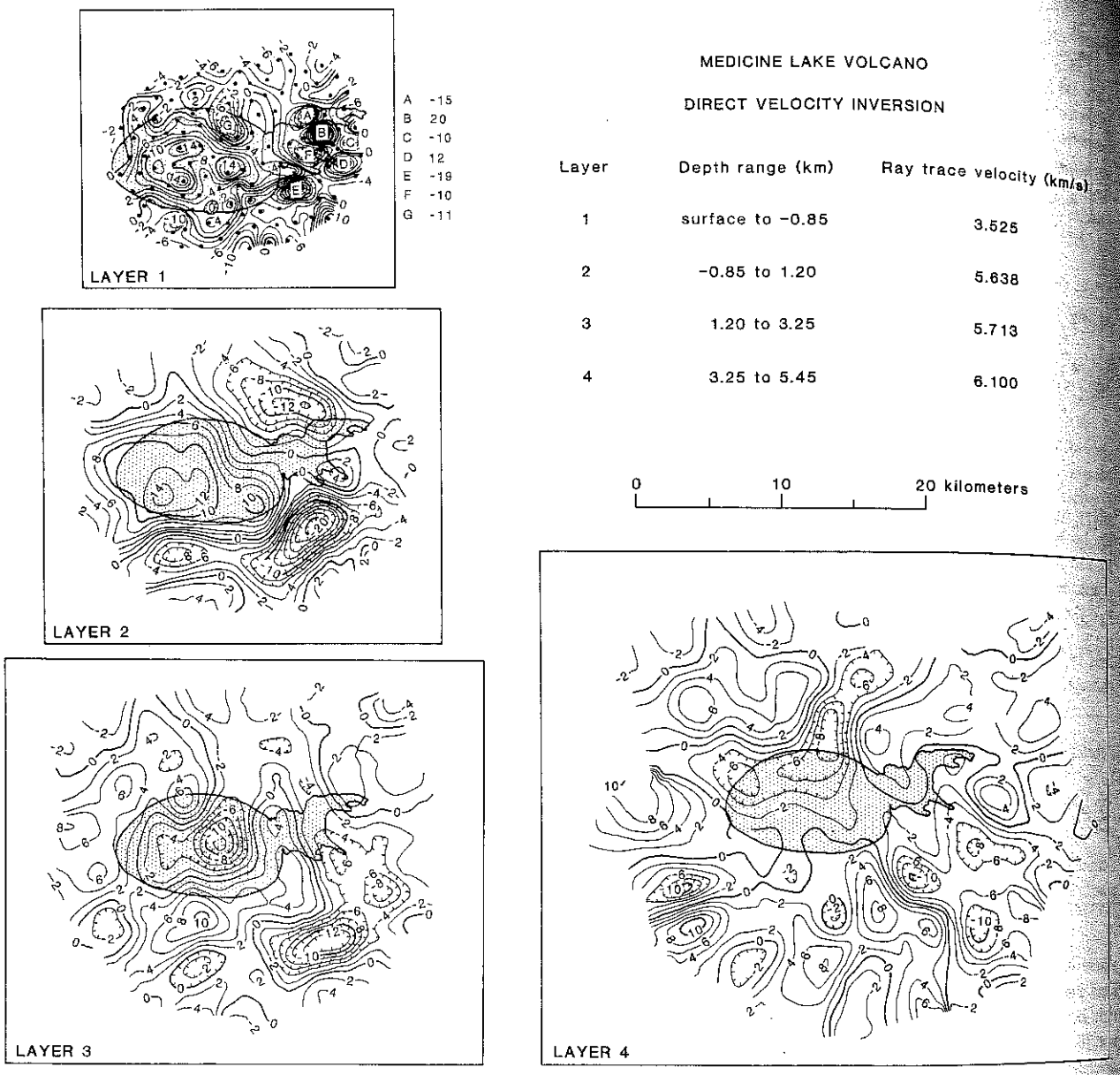

Fig. 7. Velocity perturbation model for linear best fitting residuals of Figure 6. The map view of each of the four layers is labeled by layer depth interval and ray trace velocity. The velocity contour interval is 2% of the mean layer velocity. Block boundaries are omitted for clarity.

ure 10 is effected. The numbers shown in Figure 10 are the number of offset model blocks which include that volume and also include the volume of the averaged-model block labeled 9. This averaging kernel is symmetric, smooth, centered on the averaged-model block, and without side lobes. It only smooths horizontally, however; layer thicknesses are the same for the offset models and the smoothed models.

The first layer of each model is an exception to the block structure of the other layers. In that layer a separate "block" is assigned to each seismograph, and only rays arriving at that seismograph are included in the data for that block. This strategy is consistent with the fact that the rays from neighboring sites generally do not intersect in the first layer and with the tendency of the very shallow structure immediately beneath a seismograph to dominate the velocity perturbations in the first layer. These separate blocks effectively are static terms for the sites. In the smoothed model, the nine coincident blocks beneath each seismograph simply are averaged.

The variance of the data typically is reduced by about 94% by each of the offset model inversions used to generate Figure 7, using (14). Standard deviations of the velocity perturbation estimates (i.e., the square roots of the diagonal elements of the covariance matrix) in these offset models generally are about 3% but reach about 4% in places. Diagonal elements of the resolution matrix range from about 0.5 to 0.8 in the areas interpreted below. Columns of the resolution matrix, which act as averaging kernels between the "real" Earth model m and the inversion result $\hat{m}$, are fairly compact for the important parts of the model. Thus features about 2 km across or larger and with velocity perturbations significantly larger than the standard deviations should be well resolved and interpretable. *Ellsworth* [1977], among others, defines the resolution and covariance matrices.

The main feature in Figure 7 is the large region of high-velocity material beneath the caldera in layers 1 and 2. This structure is the source of the early arrivals in the caldera. It is

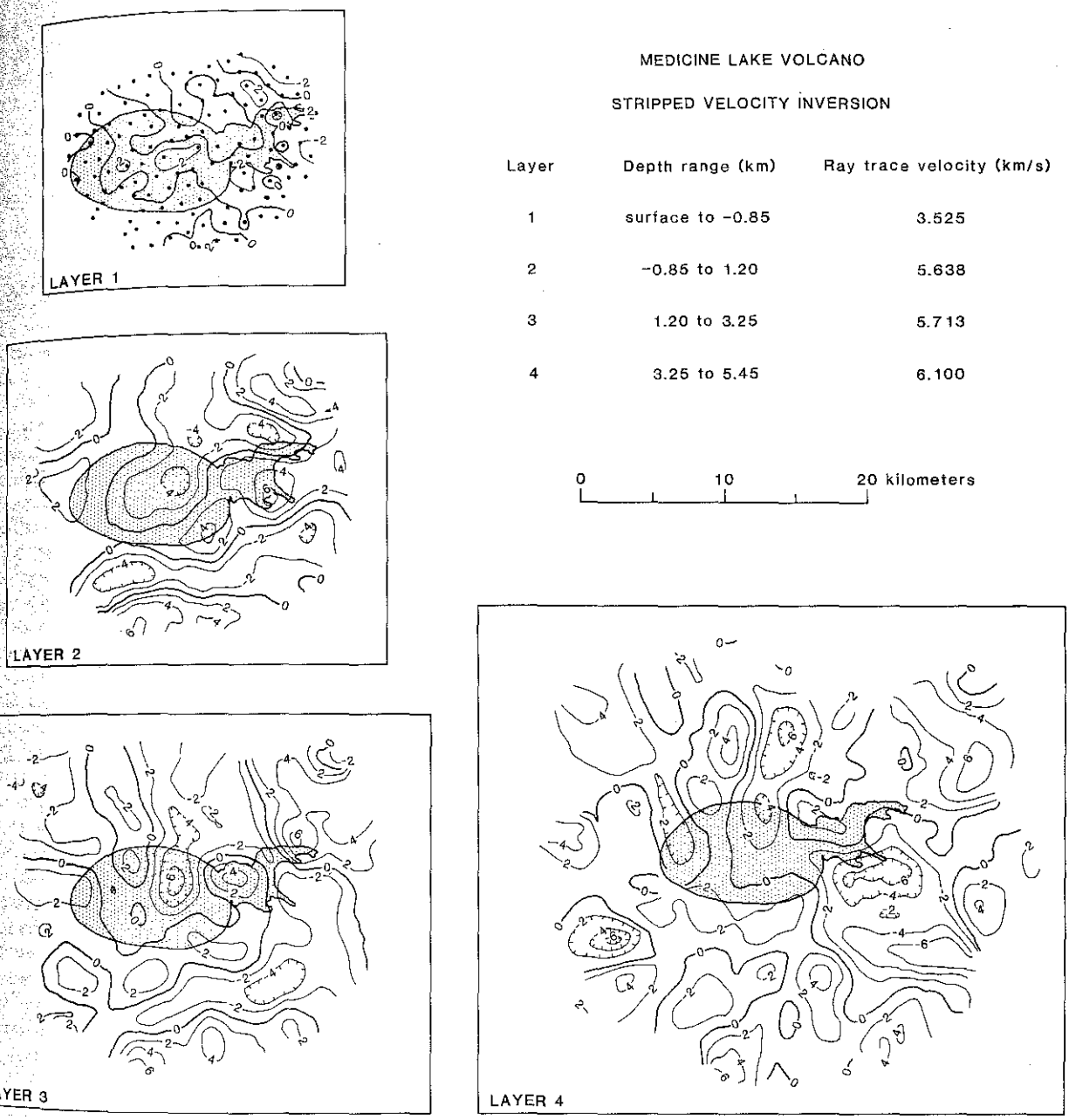

Fig. 8. Velocity perturbation model stripped of shallow structure (see text). This figure is the same format as Figure 7.

relatively formless, exhibiting no hint of the ring shape seen at Newberry volcano. Its maximum is in the western caldera beneath Medicine Lake, but nearly the whole caldera is fast in layer 2.

Layer 2 corresponds to the depth range in which *Zucca et al.* [1986] model their high-velocity anomaly (Figure 9). They observe a wide-angle reflection near the bottom of our layer 1 for sources in the caldera. Velocities above this reflector are low, so they model our layer 1 depth range as a relatively homogeneous zone above the caldera high-velocity anomaly. However, the degree of homogeneity in layer 1 is resolved by neither their work nor ours. It is known from inversions of synthetic residuals that a flat-lying lens of fast or slow anomalous material is resolved poorly in some ways by ACH inversions. Imagine a point just above or below the center of such a horizontal lens. Every ray passing through that point also passes through the lens because there are no horizontal rays in the data. Thus the data contain little or no information to determine that the point near the lens is not just as anomalous as the lens itself. In practice, horizontal lenses are modeled correctly at their edges, where unperturbed rays do pass above and below the lens after just missing it, but the center of the lens is modeled as a thicker weaker feature than it actually is. This effect is less severe with less steep incidence angles but always is present unless turning points are available above and below the lens. Thus, since Zucca et al. model the first layer as a low-velocity region, we believe that the high-velocity caldera structure in our layer 1 is partly or completely a lens artifact due to structure actually occurring in layer 2. The "stripped" model discussed below supports this conclusion.

The other major features of Figure 7 are the strong low-velocity anomalies southeast and northeast of the caldera in

TABLE 1. Initial Model for Inversions

Layer	Thickness, km	Horizontal Block Size, km × km	Initial Velocity, km/s
1	*	†	3.5250
2	2.05	2.05 × 2.05	5.6375
3	2.05	2.05 × 2.05	5.7125
4	2.20	2.20 × 2.20	6.1000

*Layer thickness equals site elevation referred to a datum at 850 m. The average layer thickness is 1.14 km.

†The region beneath each station is treated as a "block" specific to that station.

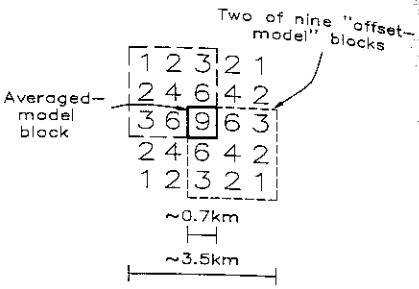

Fig. 10. Schematic illustration of the averaging kernel effected by offset-and-average process used to smooth layers 2–4 of Figures 7, 8, and 13. The numbers shown are the number of offset model blocks which include that volume and contribute to the average reported for the central block of the kernel (labeled 9).

layer 2. These features are part of a ring of low-velocity material surrounding the whole volcano, except for the western end where we have no data (it is outside the array) and the eastern end beneath Glass Mountain. We interpret this pattern of low-velocity material as the flows, tephra, and sediments making up the bulk of the volcano. The paucity of Holocene vents overlying these anomalies and the absence of Holocene vents above the most anomalous region argue against interpreting the anomalies as magmatic features. The presence of normal faults in the area, including the inferred east-down Gillem fault beneath the summit region of Glass Mountain [*Donnelly-Nolan*, 1983], suggests instead that these major features are low-velocity flank materials ponded against the downthrown side of the Gillem fault. Our modeled velocity contrast between the caldera and the southeast minimum (35%) approximately matches the contrast between *Zucca et al.*'s [1986] high-velocity anomaly (5.6 km/s) and flank material (3.5 km/s). The match probably is even closer than stated because damping tends to reduce the magnitude of modeled perturbations.

If this interpretation is correct, the absence of an anomaly under the vents and flows of Glass Mountain, which should overlie the ponded flank materials too, can be interpreted as indicating the presence of a high-velocity feature there. Compared to the value anticipated for east flank material, Glass Mountain in layer 2 is about 21% fast. Thus we interpret the "normal" velocities under Glass Mountain as an eastward extension of the caldera high-velocity anomaly.

Layer 3 (Figure 7) has less intense anomalies. The low-velocity anomaly southeast of the caldera in layer 2 seems to extend to this depth. However, its position has changed, moving farther southeast, where it is on the periphery of the model beyond the edge of the array. In this location there are few if any rays crossing the ray group arriving from the southeast. This setting is very susceptible to the "radial smearing" effects often seen in the periphery of teleseismic tomography models. Thus we believe it is partly or completely a resolution artifact in layer 3. Layer 2 does have enough rays to resolve the feature reliably there.

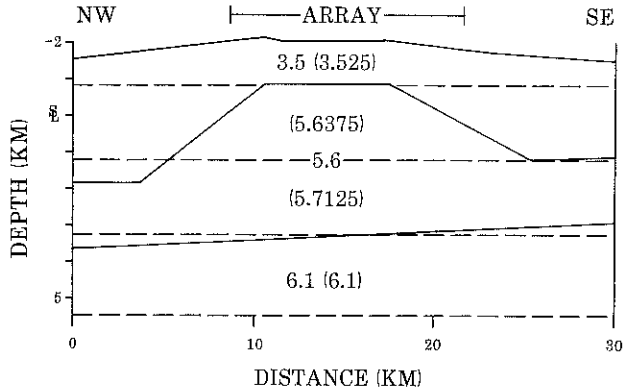

Fig. 9. Portion of Medicine Lake volcano velocity model of *Zucca et al.* [1986], also showing initial model used in ACH inversions (dashed lines and the values in parentheses). The vertical exaggeration is by 2 times.

The most noteworthy feature in layer 3 is the low-velocity anomaly in the east central caldera. This feature is the primary candidate for a silicic magma chamber in these data. Though ray coverage is good here, this interpretation is made with the following caveat. To test how well we resolve the caldera high-velocity anomaly, we performed a synthetic residual experiment. We created a data set with only shallow structure information in it by taking the average of all residuals at any given seismograph and assigning this average value to that site for all sources. Since these synthetic data now are independent of source azimuth, they should contain information only about structures too shallow to cast azimuth-dependent shadows, ideally structures in layer 1. These synthetic data were distributed with the same seismographs reporting for each source as in the real data set. The qualities assigned to the real data also were assigned to the synthetic data. (Note that even if some deep-structure contributions do not cancel fully in the averaging process, the synthetic data still contain no information implying a deep origin for the uncanceled part of such residuals. The synthetic data contain only signatures of features or parts of features for which the real data cannot discriminate depth.)

When the synthetic data are inverted, many of the features seen in Figure 7 reappear, implying the presence of resolution artifacts. In the upper two layers little difference exists between major features of the real and synthetic inversions, suggesting that we do not resolve reliably between these layers or, for that matter, between any two neighboring layers. We also note that the low-velocity anomaly beneath the caldera in layer 3 partly reappears. It matches the direct inversion much less closely than features in layers 1 and 2, but it has the same sign and about half the magnitude of that inversion's caldera anomaly.

We believe that this artifact is due to the intersection of numerous rays to sites on the flanks of the volcano, where all or most of the seismographs report delays. Thus we call this effect the "flank artifact." Stated differently, the small but finite side lobes of the resolution matrix for blocks in the caldera low-

velocity anomaly mostly are positive in the low-velocity flank regions. Thus they contribute systematically to biasing the caldera anomaly toward low velocities. The positive result of this test is that the magnitude of the real inversion anomaly is about twice that of the synthetic (about 7% slower than the synthetic data inversion).

To test whether the second layer contributes to this flank artifact, we generated another synthetic data set by ray tracing through a model corresponding to the upper two layers of the direct inversion. The velocity perturbations from the inversion were multiplied by a factor of 1.5 to compensate for damping in the ACH inversion, and these scaled perturbations were applied to the inversion's starting model to produce absolute velocities for the ray tracer. The scaling factor selected minimizes the variance of the difference between observed and synthetic residuals, creating an artificial two-layer structure with velocity perturbations in realistic locations and with magnitudes constrained by the real data. Inversion of these ray-traced two-layer synthetic residuals produced almost zero artifact in the vicinity of the layer 3 caldera low-velocity anomaly. Thus the single-layer synthetic data discussed above may even overestimate the artifact present in the direct inversion.

To eliminate or reduce the effects of such artifacts upon the deeper layers of our model, we performed the sequence of inversions which culminate in Figure 8. In this sequence, we endeavor to remove as much of the shallow structure as possible to eliminate both flank and horizontal lens artifacts. Both artifacts are caused by structure predominantly or entirely in the first two layers and should be removable by making corrections in layer 1, since these two layers mostly are unresolvable from one another.

To produce Figure 8, we first attempt to model the unstripped data used for Figure 7 with a single-layer inversion corresponding to the first layer. This single-layer inversion was iterated five times, each time adding the result of the inversion to the site correction velocity perturbation term accepted by the ACH inversion. By the fifth iteration these site corrections changed by no more than 5%, and three quarters of the sites changed by less than 1%; the correction terms generated by this procedure range from -48% to +80%.

Finally, we calculate the result in Figure 8 with the same data and initial model as for the direct inversion but removing most of the shallow structure by using the correction terms from the iterative procedure. Note that these corrections change the first-layer velocity structure through which rays are traced, moving rays by up to 0.5 km from where they fall in the direct inversion. We do not expect these changes to have a significant effect on the results. Thus the stripped model shown in Figure 8 should be the more reliable representation of the structure present in deeper layers; artifacts produced by the very strong anomalies in layer 2 should be missing from Figure 8.

"Stripping" reduces the variance of the residuals by about 85%. The variance of these stripped data typically is reduced a further 79% by the offset model inversions used to compile Figure 8. The estimated variance remaining after the stripped inversion is about half that remaining after the direct inversion. Standard deviations of the velocity perturbations in the stripped model range from 2 to 3%, and the diagonal elements of the resolution matrix range from about 0.5 to 0.7. Thus features larger than about 2 km across and exceeding about ±5% perturbation in the central parts of the model should be validly interpretable.

Layer 3 of the stripped model (Figure 8) is the most important. It retains the caldera low-velocity body which we believe may be a partial melt. The magnitude of this feature is -6.6%, which is about half that in the direct inversion and about equal to the difference between the direct and synthetic inversions. Its volume is difficult to calculate with precision. The gradational character of its boundaries and the cubic dependence of volume on radius combine to give reasonable estimates ranging from a few cubic kilometers to a few tens of cubic kilometers, depending on one's choice of boundary. Given the modeling uncertainties discussed below, we state with confidence only that this study limits the volume of the magma chamber to less than a few tens of cubic kilometers.

Thus the feature is similar in depth, volume, and magnitude to the feature observed beneath Newberry volcano's caldera by *Stauber et al.* [1985]. It also partly underlies the high-velocity lens of layer 2 (Figure 7) and therefore is not likely to be caldera-filling collapse breccia or similar low-velocity subsolidus material. It is possible that this feature represents an older flow, sediment, or tephra ponding from the volcano's youth, but the fact that there is only one and that it is roughly centered in the caldera argues against a fortuitous subsolidus feature and in favor of a feature somehow related to caldera formation. We interpret this feature, therefore, as a small magma chamber.

Layer 2 of the stripped model (Figure 8) largely lacks the high-velocity anomaly so prominent in layer 2 of Figure 7. Clearly, the stripping exercise has removed much of the structure that was causing artifacts in the model. It is worth noting, however, that Figure 8 indirectly supports our belief that most of the caldera high-velocity anomaly is in layer 2, rather than layer 1. Recalling that the edges of horizontal lenses are resolved correctly, note that there is a ring of higher velocities beneath the caldera boundary. We suggest that this ring is the edge of the caldera high-velocity anomaly, left behind by the stripping process. This edge is depth resolvable, is not pulled into layer 1, and thus is not removed from Figure 8. Its presence in layer 2 supports our contention that the lens is in layer 2.

In practice, the bottom layer of any ACH inversion should be disregarded or interpreted with great care. This layer acts as a kind of dump for structure outside the modeled volume but close enough to it to produce observable residuals. In this experiment, the ray bundles from the eight sources also largely are separated from one another in layer 4, seriously reducing the resolution of structures in this layer. For these reasons, we do not attempt any interpretations based on this bottom layer.

One final note is relevant. When we invert residuals calculated using the a priori apparent velocities discussed above, the positions of the rays change significantly. In the first and second layers, the rays change position by only 0.05 km and 0.73 km, respectively, in the centers of the layers. However, layers 3 and 4 sustain changes of over 2 and 5 km, respectively. Thus the rays which contribute to the caldera low-velocity anomaly in layer 3 are substantially spread out compared to the rays in the preferred inversions. One effect is that the caldera low-velocity anomaly vanishes from the a priori inversions. (The major features in layer 2 are little affected, so the structural conclusions drawn below from these are firm.)

The points favoring the presence of a caldera low-velocity anomaly in layer 3 are (1) the arguments given above favoring best fitting residuals and slownesses over a priori residuals and slownesses, (2) the persistence of the feature in the stripped model, and (3) the signature, discussed below, of an attenuator in the same location. This attenuator is observed both directly

in δt^* data as well as in inversions of these data. The points against the anomaly are (1) the absence of a clear signature for this feature in the travel time residuals (Figure 6), (2) the absence of the feature in inversions of the a priori residuals, and (3) the presence of resolution artifacts in the same location. Thus, while we believe the caldera low-velocity feature is real, its existence is not certain. At the least, however, these results place an upper bound on such features.

In summary, we believe that layer 1 contains no resolvable high-velocity anomaly [*Zucca et al.*, 1986], that layer 2 is represented best in Figure 7, that layer 3 is represented most accurately in Figure 8, and that layer 4 should not be interpreted. The major structures seen in these inversion models are (1) the caldera high-velocity lens in layer 2, (2) the east-west elongation of this high-velocity lens including the relatively high velocities beneath Glass Mountain, (3) the ponding of subsolidus low-velocity materials against the Gillem fault under the east flank of the volcano, and (4) the caldera low-velocity anomaly in layer 3, which may be a small magma chamber. In the next section we develop attenuation information for these features, and in the final section we jointly interpret these results.

COMPRESSIONAL WAVE ATTENUATION STRUCTURE

In this section we compute the attenuation structure of the target volume using the t^* method. Attenuation information is complementary to velocity data; the two can be used together to strengthen an interpretation. Many mechanisms have been proposed to explain attenuation of seismic waves. Small amounts of partial melting [*Mavko*, 1980] are a likely source of attenuation in a volcanic regime. Pores also are likely to be open at these shallow depths, and the effects of water and water vapor can be substantial as well [*Ito et al.*, 1979]. We will use these mechanisms to explain some of our results.

Method

To compute attenuation structure we use the body wave equalization procedure developed by *Teng* [1968]. Since that study, the method has been used primarily to investigate attenuation structure using teleseisms [*Taylor et al.*, 1986; *Ward and Young*, 1980; *Solomon and Toksoz*, 1970]. Our technique basically follows these past studies with some minor modifications.

The amplitude spectrum at seismograph i from source j can be written [*Teng*, 1968]:

$$A_{ij}(f) = A_j^0(f)A_j^r(f)A_{ij}^u(f)A_i^s(f) \tag{15}$$

where f is frequency. A_j^0 is the source spectrum and is not dependent on the source-to-seismograph azimuth in the case of an explosion. A_j^r is the transfer function of the part of the Earth between the source and the target volume. A_{ij}^u is the transfer function of the upgoing part of the ray through the target volume. A_i^s is the instrument response. (This notation should not be confused with the matrix A in (10) and (12).) We assume that A_j^r is approximately the same for all ray paths from source j and that the instrument response A_i^s is the same for all seismographs (we have deconvolved all data to a common instrument response).

In most studies, a reference seismograph outside the area of interest is used to form the denominator of the spectral ratio. Instead we use the average log spectrum per source,

$$\overline{\ln A_j} = \ln A_j^0 + \ln A_j^r + \ln A_i^s + \frac{1}{I_j}\sum_{i=1}^{I_j}\ln A_{ij}^u \tag{16}$$

for reasons discussed below. The spectral ratio, i.e., the log difference, is given by

$$\ln S_{ij} = \ln A_{ij} - \overline{\ln A_j} = \ln A_{ij}^u - \frac{1}{I_j}\sum_{i=1}^{I_j}\ln A_{ij}^u = \ln A_{ij}^u - \overline{\ln A_{ij}^u} \tag{17}$$

since A_i^s and the terms that depend on the source cancel. We have defined the term $\overline{\ln A_{ij}^u}$ to be the average of the upgoing parts of the ray. A_{ij}^u can be factored in the following manner [*Teng*, 1968]:

$$A_{ij}^u = \gamma_{ij}\exp\left[-f\left(t_{0,ij}^* + \delta t_{ij}^*\right)\right] \tag{18}$$

where γ_{ij} is the geometrical spreading factor and is independent of frequency. The quantity t^* is given by

$$t^* = \pi\int_{\text{ray}} Q^{-1}v^{-1}ds \tag{19}$$

where Q is the quality factor and v is the P wave velocity. Equation (19) is linear in Q^{-1} but not in Q, so one may write

$$t_0^* + \delta t^* = \pi\int_{\text{ray}}\left(Q^{-1}+\delta Q^{-1}\right)\left(v_0^{-1}+\delta v^{-1}\right)ds \tag{20a}$$

We assume that δQ^{-1} is much larger than δv^{-1} so that we can ignore terms containing δv^{-1} and write

$$\delta t^* = \pi\int_{\text{ray}}\delta Q^{-1}v_0^{-1}ds \tag{20b}$$

Using (18) to rewrite (17), we have

$$\ln S_{ij} = f\left[-t_{0,ij}^* + \frac{1}{I_j}\sum_{i=1}^{I_j}t_{0,ij}^*\right] + f\left[-\delta t_{ij}^* + \frac{1}{I_j}\sum_{i=1}^{I_j}\delta t_{ij}^*\right] + C_{ij} \tag{21}$$

The C_{ij} are constants which depend on variations in geometric spreading and instrument gain. Since we assume that the ray paths have the same mean t^*, we may write

$$\ln S_{ij} = C_{ij} - f\,\delta t_{ij}^* + \frac{f}{I_j}\sum_{j=1}^{I_j}\delta t_{ij}^* = C_{ij} - f\left[\delta t_{ij}^* - \overline{\delta t_j^*}\right] \tag{22}$$

The quantity that we measure is the slope of the curve which is the second term in (22). Our formulation is similar to that of *Young and Ward* [1980] except that we reference our measurements to the average spectrum for the source rather than to a single reference seismograph. Mathematically, this is equivalent to subtracting the average δt^* as did *Taylor et al.* [1986]. The advantage of our method is that the average spectrum usually is smooth and without spectral holes, caused by the site response of the reference station, which can distort the spectral ratio.

Since δt^* can be written as a ray path integral, we may use the ACH inversion routine, just as for the velocities. In this case we parameterize the medium (compare equation (2*a*)) with

$$\delta m_k = \pi\delta Q^{-1}\delta_k$$

Equation (20*b*) becomes

$$\frac{\delta t^*}{\delta m_k} = \pi\int_{\text{ray}}\frac{1}{v_0}\frac{\delta Q^{-1}}{\delta m_k}ds$$

For a given seismograph i and source j, the measured δt^* is

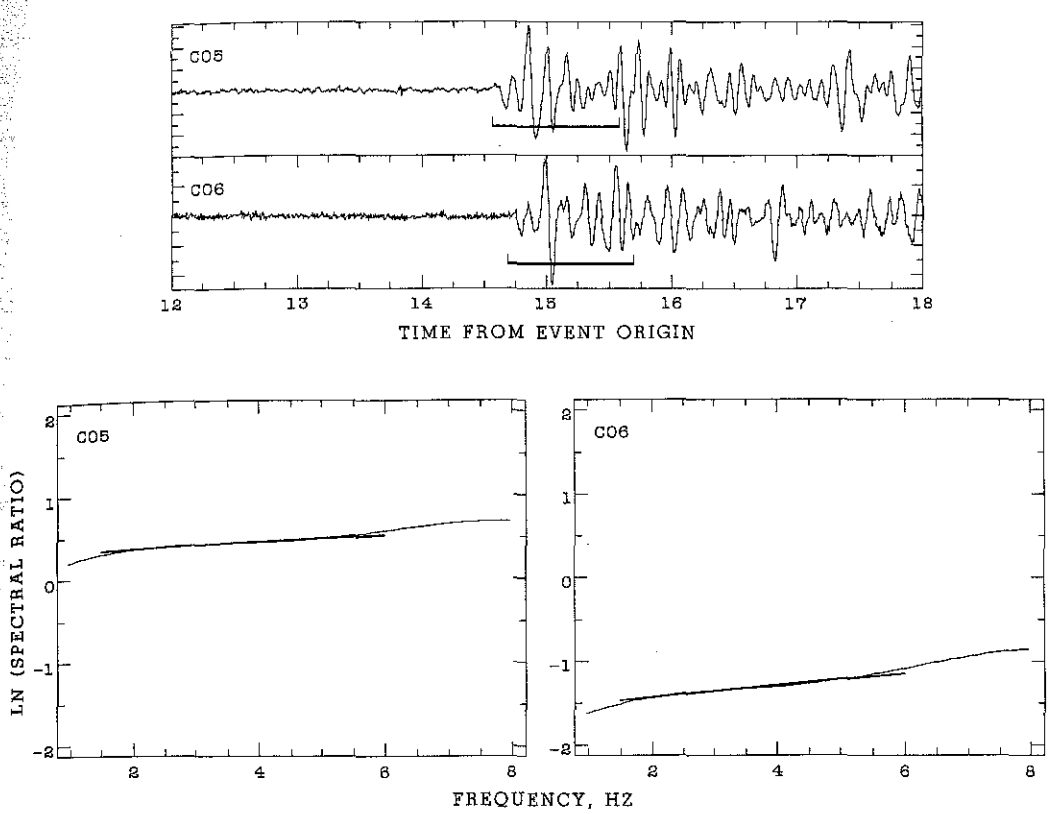

Fig. 11. Example of data used to calculate δt^*. (Top) Sample seismograms from source number 4. The window over which the spectrum is calculated is shown by the bar. (Bottom) Spectral ratios calculated using the above seismograms. The station name is indicated in the upper left corner. The negative of the slope of the line, which indicates the least squares fit to the data, is δt^*.

$$\delta t_{ij}^* = dO_j + \sum_k \left\{ \pi \int_{\text{base}}^{\text{seismograph } i} \frac{1}{v_0} \frac{\delta Q^{-1}}{\delta m_k} ds \right\} \delta m_k + e_{ij} \quad (23)$$

where e_{ij} is an error term and dO_j is introduced to account for unresolvable terms (C_{ij}) that may be present, as before in the travel time case. Equation (23) is similar to (3) of the travel time case. As before, the quantity in braces is equal to the unperturbed travel time in each block. In this case, however, we invert directly for δQ^{-1} rather than for $-\delta v/v_0$ as in the velocity case. Furthermore, the δt^* inversion is carried out over the same ray paths as the direct velocity inversion, since we use the same starting model.

Calculation of δt^*

To calculate δt^* for each ray, we use the travel time picks from the first part of the study to define a window around the first arrival. The choice of the window size is critical to the success of the attenuation study. A window that is too large certainly will contain secondary arrivals that will not have traveled the same path as the first arrival and therefore will distort the data. If the window is too short, an accurate estimate of the spectrum cannot be made. We chose a window length of 1 s (Figure 11, top); a window this size contains several cycles of the dominant frequency of the signal and, at frequencies below 6 Hz, probably does not contain energy that has been laterally scattered. The 6-Hz limit for scattered energy was determined by *Saltzman et al.* [1987]. They used the three-component Medicine Lake data to show that the particle motions of the first several cycles of the P wave point back toward the source but that above 6 Hz the particle motions point significantly away from the back azimuth. This finding suggests that lateral scattering is not significant below 6 Hz.

Another potential problem is separating the effects of intrinsic and scattering attenuation. Scattering tends to shift the high-frequency content of the initial pulse into the coda [*Richards and Menke*, 1983]. We looked for this effect by comparing the peak in the spectra for three overlapping 1-s windows starting at the P wave arrival and with a lag between windows of 0.5 s. We observed no consistent pattern. The highest peak frequency was distributed randomly between all three windows. Without a doubt, significant scattering is occurring in our data as evidenced by the rather long P codas (Figure 11, top). However, instead of biasing our results, scattering along the direct ray path probably only adds noise to our measurements of δt^*.

After windowing the data, we estimated their spectra by the maximum likelihood method. We chose this method over the fast Fourier transform because the former generally gives smoother results and is optimized to preserve the shape of the spectrum. We use a simple ensemble average for the average spectral ratio for each source.

We fit a least squares line to the natural logarithm of the spectral ratio in the 1- to 6-Hz band. The negative of the slope of this line is the δt^* value (Figure 11, bottom). The 1-Hz limit is dictated by the window length. The 6-Hz limit was chosen to minimize the effects of scattered arrivals.

By this method, we produce δt^* values for all i and j. In spite of the averaging done to the denominator in the spectral ratio, the raw data set appears noisy, and inversions of it yield little variance reduction. To smooth the data, we applied a

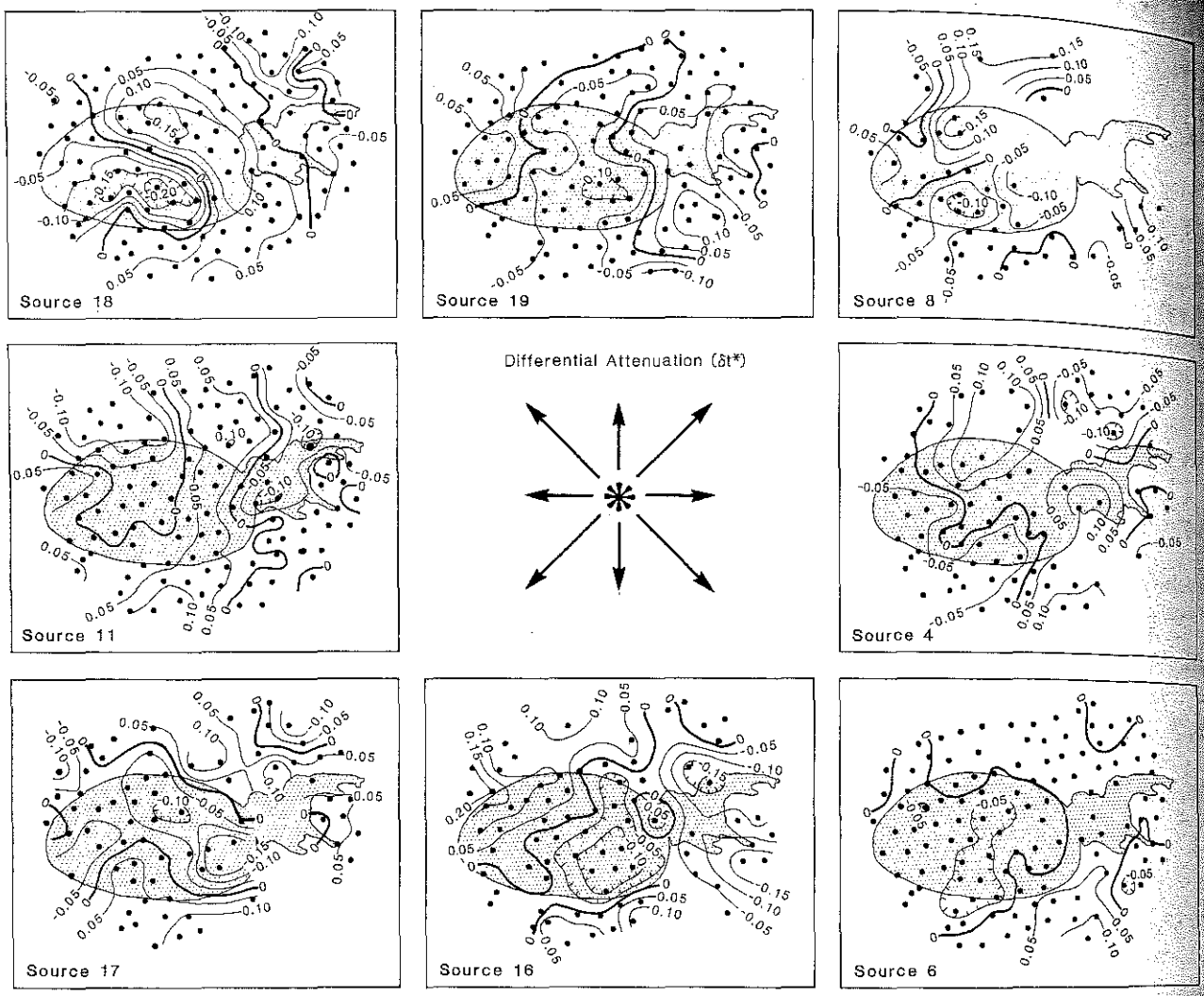

Fig. 12. Plot of δt^* data filtered by a median window of 1.754-km radius, a distance chosen to include the nearest ring of neighboring stations. The purpose of the filtering was to despike the data. The format is the same as for Figure 6.

median filter because this kind of nonlinear filter discriminates against the spikes evident in the data [e.g., *Evans*, 1982*b*]. For each source, the value at each site is replaced by the median of that value and the values for the same source for all seismographs within 1.754 km, a distance selected to encompass the hexagon of nearest neighbors. This filtering may smooth some of the anomalous regions and therefore may obscure some finer details; however it will not broaden such features the way a linear filter can.

Interpretation of δt^* Data

Median-filtered δt^* data are shown in Figure 12 for all sources. These data may be interpreted qualitatively in the same manner as travel time residuals, with relatively attenuating regions casting positive shadows and less attenuating regions causing negative patterns.

The data are complexly source-azimuth-dependent; however, all or part of the caldera is negative for all sources, suggesting that some shallow high-Q material lies beneath it. This material may coincide with the high-velocity lens in layer 2, though its signature is far less distinct than in the velocity model.

Three azimuth-dependent patterns can be seen: high-attenuation patterns centered in the eastern half of the caldera and southeast of the caldera and a high-Q pattern centered on the northern caldera boundary, more or less at Mount Hoffman (Figure 3). The eastern caldera feature appears as positive patches in the north caldera for source 18, the west caldera for source 11, possibly the south caldera for source 17, south of the eastern caldera for source 16, south of Glass Mountain for source 6, on Glass Mountain for source 4, and possibly on the northern fringe of the array for source 19. Too few data are present for source 8 where this feature is expected. The movement of this shadow and its symmetry about the eastern caldera suggest that it derives from the same region as the caldera low-velocity anomaly in layer 3.

The attenuating feature southeast of the caldera, i.e., south of Glass Mountain, appears as the positive regions south of the caldera for sources 11 and 17, on the southeast fringe of the array for source 6, possibly at the southeast corner of Glass Mountain for source 8, south of Glass Mountain for source 19, and as the eastern part of the broad positive area in the northern and eastern caldera for source 18. This feature evidently is shallower than the eastern caldera feature (the shadow does not move as far) and underlies the southeast part of the array. It probably coincides with the southeast low-velocity flank ano-

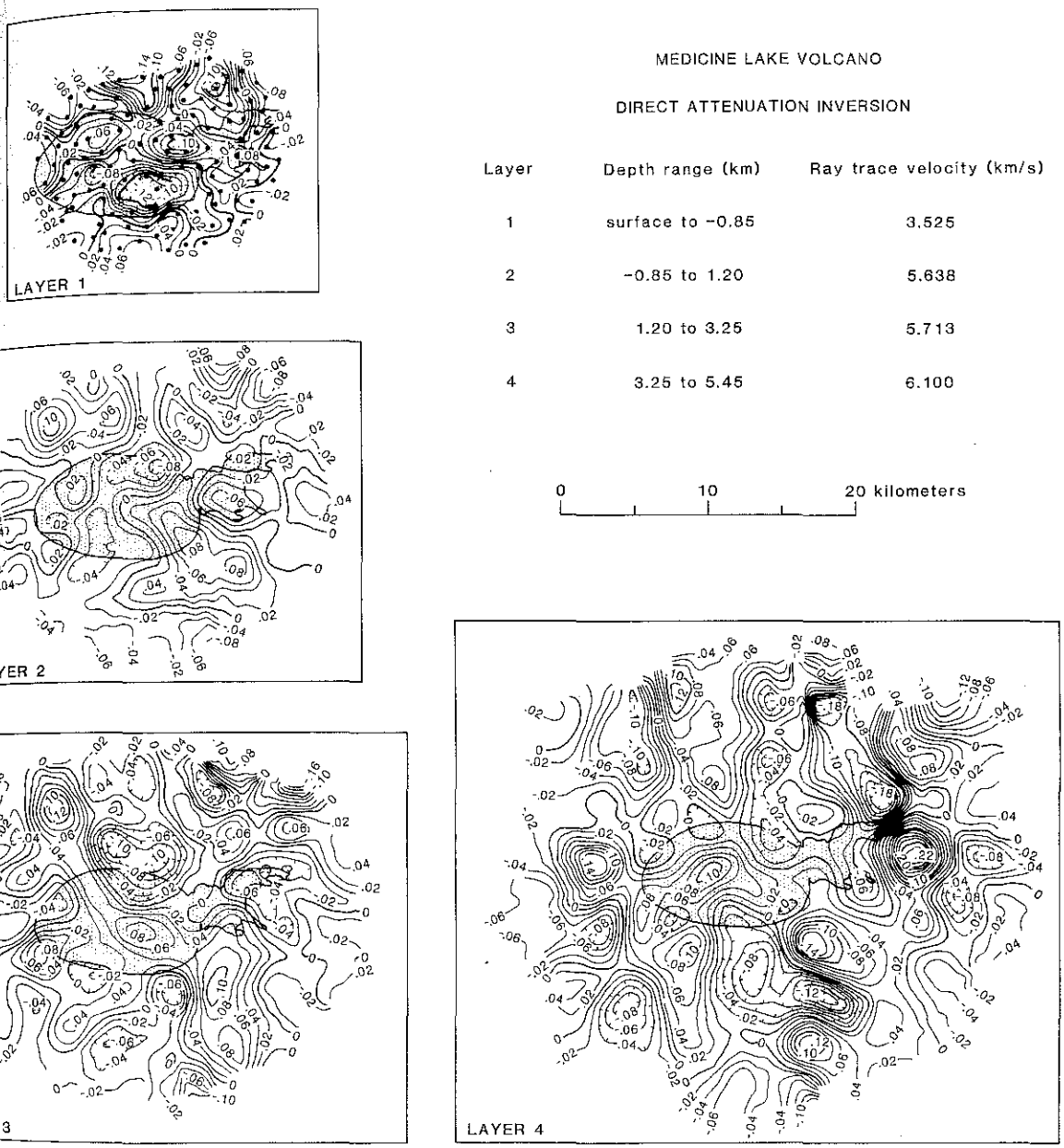

Fig. 13. Model of $\pi\delta Q^{-1}$ for median-filtered δt^* data shown in Figure 12. The value of $\pi\delta Q^{-1}$ is proportional to attenuation, which implies that areas of positive $\pi\delta Q^{-1}$ (i.e., low Q) are more attenuative.

maly, though it may be centered somewhat deeper than that feature.

The high-Q feature centered on the northern boundary of the caldera is visible as negative patches at the northwest corner of the array for source 11, the northwest caldera for source 17, and the southeast caldera for source 16. It also may be visible north of Glass Mountain for source 4 and as the eastern part of the broad caldera low for source 6. The anomalous high-Q volume probably is located in layer 2 or 3 beneath Mount Hoffman and does not correlate with any first-order velocity feature.

Inversion for Attenuation Structure: Results

The results for the attenuation inversion are shown in Figure 13. As for the velocity case, the inversion model requires explanation to understand its significance. In the first place, the δt^* data do not require the stripping procedure used above. The stripping is important for velocity models because strong shallow anomalies can bias the model in certain regions, such as the center of the caldera. In the attenuation case, we do not have these very strong signals from shallow structure, and the stripping procedure is not required.

The data used in the inversions are those discussed above for Figure 12. In contrast to the velocity case, no weighting is used for the data because the median filtering is believed to account adequately for variations in data quality. The same initial velocity model was used in this inversion as in the velocity case. We applied the offset-and-average smoothing algorithm to produce the inversion in Figure 13. The variance of the data typically is reduced by about 84% by the inversions that make up the offset-and-averaged model. Compare this with 94% for the velocity models.

For comparison, we also inverted the raw, unfiltered data with the offset-and-average technique. Because of space considerations these data are not shown, but we will refer to them in this section.

The inversion results are presented as variations in $\pi\delta Q^{-1}$. Positive $\pi\delta Q^{-1}$ indicates areas of high attenuation or low Q. Negative $\pi\delta Q^{-1}$ indicates the opposite: low attenuation or high Q. Low or high attenuation is measured relative to some average Q for the region. As in the velocity case, we do not know the average Q; we can only measure variations in Q^{-1}. We can discuss, however, the amplitude of variations in Q that could cause the variations that we observe in δt^*. For example, if the average Q is 100, a Q of 10 in layer 2 (5.6375 km/s in Figure 9) is required to produce a δt^* of 0.20, which is the order of the δt^* values that we observe (Figure 12).

The main feature in layer 1 of the attenuation model (Figure 13) is that the southern part of the caldera is less attenuating than the northern part while the flanks have the characteristic noise oscillations, indicating no clear anomaly pattern (compare the section on results of inversion for velocity structure). The caldera high is coincident with the Lake Basalt of *Anderson* [1941] and may represent a feeder complex for one of its vents, or simply an unrelated buried feature.

The main feature in layer 2 is the low-Q zone in the southeast part of the image and extending into the southeast part of the caldera. This structure is the source of the clearest negative δt^* anomaly discussed above for the data (Figure 12). In the inversion for the unfiltered data the anomaly appears slightly separated at the caldera rim. The low-Q region outside the caldera correlates with the strong velocity low southeast of the caldera (Figure 7). As discussed above, this Q and velocity low is part of a larger ring around the flanks of the volcano. It is particularly strong here in both velocity and attenuation. The other low-Q zones in layer 2 also correlate with this low-velocity ring. These include the weak low-Q zones northwest, north, and northeast of the caldera rim. Two weaker anomalies are the high-Q zones under the northeast portion of the caldera rim and beneath Glass Mountain. The northeast rim anomaly does not correlate with anything in the velocity image, but the high-Q zone under Glass Mountain correlates with the inferred velocity high in this region. The rest of layer 2 contains no interpretable anomalies in our opinion.

In layer 3 the strong anomaly southeast of the caldera still is visible and here has a distinct north-south elongation. As in the velocity case, we must interpret at least the southern part of this feature as being the result of radial smearing, though the northern part may be a real feature. The other flanking lows also are present at this depth but are less sharply imaged, suggesting that lateral smearing is a factor here too. The primary feature of interest in layer 3 is the low-Q zone in the center of the caldera; it correlates very well with the central caldera low-velocity zone (Figure 8). This anomaly can be seen directly in the δt^* data as discussed in the previous section. Though a similar pattern is difficult to discern directly in the travel time residuals (Figure 6), it is apparent in all inversions as well as in the δt^* data themselves. Thus we believe these results demonstrate that the feature is real, notwithstanding the uncertainties discussed in previous sections.

The high-Q zone on the northwest rim of the caldera which is faint in layer 2 appears as a strong feature in layer 3. Again note that this feature has no obvious analog in the velocity image (Figure 7).

For the same reasons as in the velocity case, we do not interpret the results for layer 4. We present the inversion results in Figure 13 only for completeness.

In summary, the major features of the attenuation inversions are as follows: (1) In layer 2 there are flanking low-Q zones which correspond to the flanking low-velocity zones in the velocity image. These zones are strongest in the southeast. (2) Also in layer 2 there is a low-Q zone just inside the caldera south of the Hoffman flows. (3) In layer 3 there is a low-Q zone in the central part of the caldera which correlates with a low-velocity zone. (4) Also in layer 3 and more weakly in layer 2 there is a high-Q zone located beneath Mount Hoffman on the northeast rim of the caldera. This high-Q feature does not correlate with any obvious feature in the velocity image.

DISCUSSION

Plate 1 shows in color the key inversion results from Figures 7, 8, and 13 in a format facilitating comparison of velocity and attenuation structures. (Plate 1 can be found in the separate color section in this issue.) Figure 14 shows our structural interpretation of Plate 1. This section describes how we arrive at this structural interpretation from a joint evaluation of velocity, attenuation, and other information and what reliability we ascribe to its features.

The velocity and attenuation patterns in Plate 1 can be ascribed to differences in rock type, including porosity differences, and to differences in the state of pore fluids in these rocks. *Ito et al.* [1979] describe a steam-water transition experiment upon which we base much of our joint velocity-attenuation interpretation. Their experiment was performed at 30 MPa confining presure, equivalent to about 1.4 km below surface for Medicine Lake volcano (ρ~2.2 g/cm^3). They varied pore pressure at constant temperature to produce steam-saturated, water-saturated, and transitional pore fluid conditions. In general, they found that P wave velocity is highest in water-saturated conditions and lowest in transitional conditions. P wave Q generally was lower in water-saturated than in steam-saturated samples. At some temperatures, Q showed a marked minimum in the transitional state. *Ito et al.* [1979] attributed velocity variations to changes in bulk compressibility and density of the sample due to addition of water. The Q minimum was attributed tentatively to either local flow effects or thermal relaxation. These results are illustrated schematically in Figure 15 for a competent rock (two top curves) and a porous low-velocity rock (two bottom curves). We also use the results of partial melt models [e.g., *Mavko*, 1980].

Referring to Plates 1*a* and 1*c*, note that the major low-velocity feature southeast of the caldera in layer 2 coincides with a low-Q anomaly. We interpret this feature as porous materials erupted and eroded from the volcano and deeply ponded on the downthrown (east) side of the Gillem fault. Thus we attribute the anomaly to intrinsically low velocities and low Q exhibited by such porous incompetent materials. We presume they are below the water table, which should be near the elevation of Tule Lake (D. Adam, personal communication, 1988), and saturated with water (flank in Figure 15).

At the same depth, the caldera high-velocity anomaly (Plate 1*a*) does not coincide with any significant caldera-wide Q anomaly, in spite of the weak caldera-wide high suggested in the qualitative discussion given above for δt^* data. Indeed, Q in the caldera in layer 2 is patchy with an average near the average outside the caldera. The region directly beneath Medicine Lake

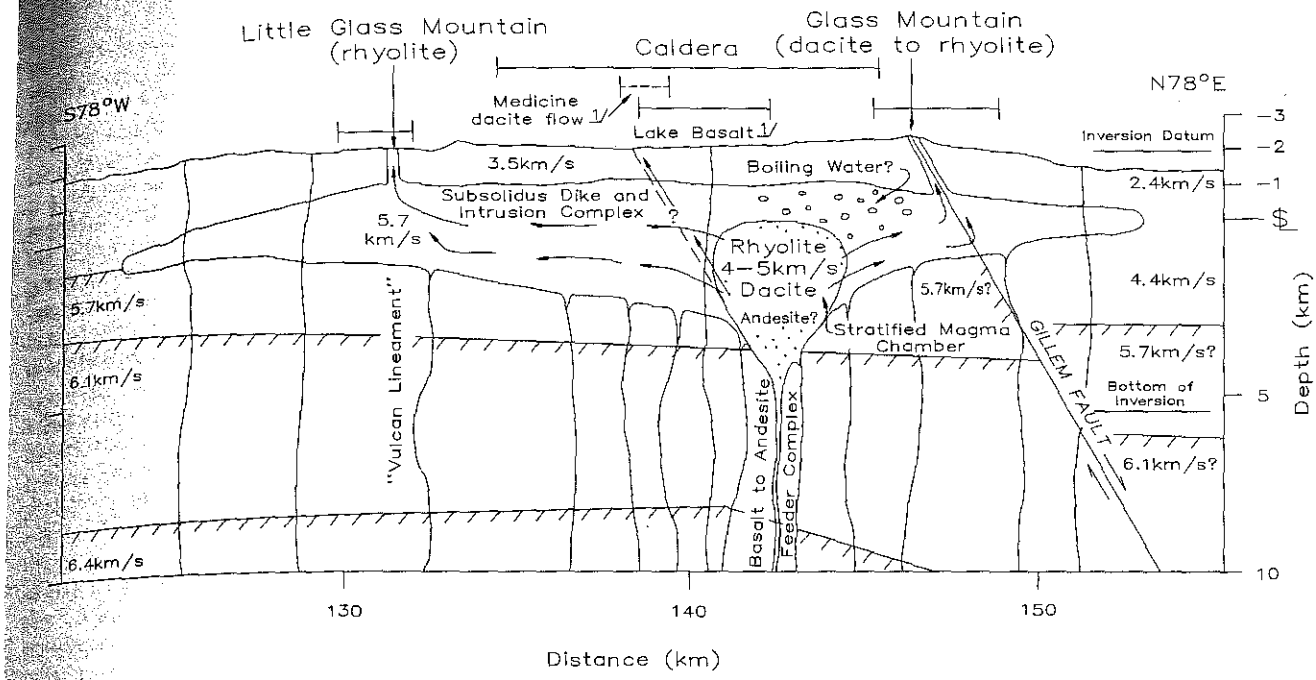

1/ of *Anderson* [1941]

Fig. 14. Interpretive model of Medicine Lake volcano along a section striking N78°E between Little Glass Mountain and Glass Mountain. There is no vertical exaggeration; the distance scale is the same as that of *Zucca et al.* [1986, Figures 15 and 17]. The bars show flow positions; Medicine dacite flow is out of section to the north. Many details are only schematic. Flow arrows show inferred magma paths during the youngest silicic eruptions. The magma chamber is drawn near the upper limit of possible volumes; it may be smaller.

probably has a slightly elevated Q and may correlate with the fastest part of the caldera high-velocity anomaly. The correlation is tenuous, however, and we attribute this pattern to relatively competent water-saturated rock (caldera in Figure 15). Such material can have very high velocities while maintaining an average Q. It should be noted that the region beneath Glass Mountain previously interpreted as a relative high-velocity feature does show high Q as well. In contrast to expected low-Q east flank materials, the intrusive complex we attribute to this area should have such a signature. The Glass Mountain high-Q anomaly supports our assertion that the caldera intrusive complex extends east from the caldera to this region.

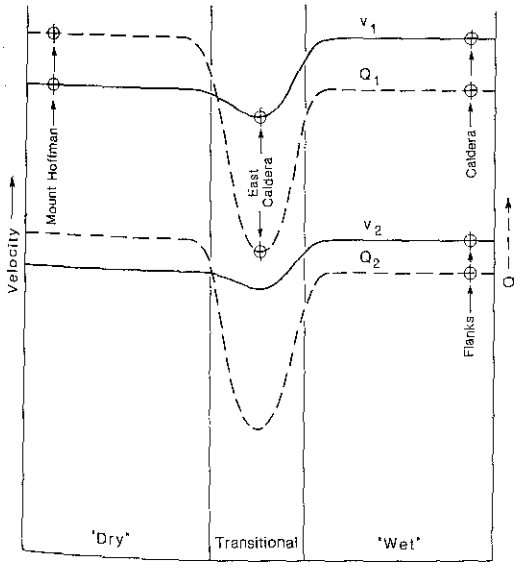

Fig. 15. Schematic illustration of velocity and attenuation response of porous rocks at low confining pressures, rendered from *Ito et al.* [1979, Figures 2, 4, and 7]. The upper two curves are for competent rocks with higher intrinsic Q and velocity.

The eastern caldera in layer 2 is the only significant low-Q region in the caldera at this depth. It corresponds to a high-velocity region. Figure 15 (east caldera) suggests a possible mechanism for resolving this apparent contradiction by introducing partial pore-fluid saturation. Both the velocity and Q are lowered, though the velocity may still be higher than in the flank materials. As shown schematically in Figure 15, the data of *Ito et al.* [1979] suggest that the decrease in Q is greater, even by an order of magnitude, than the decrease in velocity when expressed as a fractional change. Thus a significant Q anomaly might be produced without substantial change in the velocity field. We suggest that the eastern caldera in layer 2 is partially saturated with water, perhaps boiling water. Water can boil anywhere in layers 1 or 2, since the critical point of water is at 21.8 MPa, or a hydrostatic head of about 2.2 km. Thus the critical point should be about 2.2 km below the elevation of Tule Lake, or about 0.9 km below sea level.

A similar low-Q area northwest of the caldera in layer 2 does not coincide with a velocity anomaly. It may be another area of boiling water. It is on the fringe of the models, however, and is poorly resolved by both data sets. Thus its interpretation is tentative.

The central caldera low-velocity anomaly in layer 3 substantially coincides with a low-Q region in the same layer (Plates 1*b* and 1*d*). Above, we tentatively identified this double anomaly as a small magma chamber. The coincidence of low Q and low velocity supports this interpretation. However, it does not discriminate between melt or partial melt and the porosity source of the southeast flank anomaly in layer 2. The sugges-

tion that layer 2 contains a volume of boiling water in the eastern caldera weakly supports the presence of a magma chamber, since layer 2 could be transporting heat from the magma chamber to the porous material of the southeast flank where the steam would quench or dissipate. The strongest arguments in favor of a magmatic model remain the location of this feature inside the caldera, the lack of any evident sediment and tephra ponding mechanism (fault or collapse pipe) in that location, the absence of any other such features in the caldera (suggesting it is not just one of many older porous flows), and the coincidence of its depth with the expected depth of andesite fractionation to rhyolite [*Grove and Donnelly-Nolan*, 1986].

The last significant feature is in Plate 1*d*: the high-Q feature beneath Mount Hoffman on the northern caldera boundary in layer 3. This feature may extend into layer 2 as well but in neither layer corresponds to any obvious velocity anomaly. Indeed, it coincides with velocity gradients in both layers. We interpret this feature as a "dry" competent rock body, possibly a subsolidus silicic intrusive body or feeder complex for vents on Mount Hoffman. The intrinsic velocity of low-porosity subsolidus silicic rocks would be average for the crystalline upper crust but could still have a higher Q than the average if it contains water only in a low-viscosity state (Mount Hoffman in Figure 15). Layer 3 presumably is at a pressure above the critical point of water, but if hot, the water would be in a low-density single-phase state [e.g., *Fisher*, 1976]. Thus the region could be dry either by virtue of extremely low porosity or by being hot.

Figure 14 shows a partly schematic interpretation of these features. The figure is drawn without vertical exaggeration and shows true topography along a N78°E section passing through the main vents of Little Glass Mountain and Glass Mountain. The framework velocity structure is taken from *Zucca et al.* [1986] with modifications to show offsets along the Gillem fault. The original refraction model shows east dipping interfaces in the same area. The offset shown on the Gillem fault was chosen to give roughly correct travel times to the southeast flank, and the dip is presumed to be 60°. The vents of Little Glass Mountain are in line with the Holocene "Crater Glass flow" of *Ciancanelli* [1983] to the northeast forming part of the "Vulcan lineament". The sense of motion on this feature is of east-west opening with possible minor west-down motion in one area and possible minor east-down motion elsewhere (J. Donnelly-Nolan, personal communication, 1987). Thus we indicate it simply by name in Figure 14.

The major velocity anomalies from this study are represented by a subsolidus dike and intrusion complex, a small stratified magma chamber, and the throw on the Gillem fault. The basalt and andesite feeder complex beneath these major features is inferred from the anomalously high apparent velocity of *Pg* discussed above and from the teleseismic tomography results of *Evans* [1982*a*] and reanalysis of refraction data by R. Catchings (personal communication, 1986). A "B-type" low-frequency earthquake occurring roughly 9 km beneath Little Glass Mountain in 1986 (S. Walter, personal communication, 1987) probably was in this feeder complex. This earthquake is the only one recorded at Medicine Lake volcano in 6 years of microearthquake monitoring. It was on the edge of the seismograph network, so its location is only approximate.

The dike and intrusion complex is shown extending east beneath Glass Mountain, based on our results, and west of the caldera, based on time term analysis of refraction data by W. Kohler (personal communication, 1987) and gravity modeling by *Finn and Williams* [1982]. North and south of the caldera the complex is more restricted according to both our results and Kohler's. This east-west elongation is interpreted as a response to some crustal weakness predating the current basin-and-range style faulting. This crustal weakness probably is related to the Mount Shasta–Medicine Lake topographic lineament shown in Figure 2. The depth of the complex may be controlled in part by loss of buoyancy as magmas leave the 5.7-km/s layer and enter the low-velocity low-density upper layer. We assume that the complex is a mix of sills (perhaps along such density contrasts), dikes controlled by the lineament, and perhaps small intrusive bodies. It probably contains intrusive equivalents of all the rocks seen at the surface, i.e., from basalt to rhyolite.

More primitive magmas may pierce this complex at a number of locations, for example, to emplace the Lake Basalt within the caldera. The Lake Basalt, however, may be a cumulate rather than a primative basalt. It is also likely that the complex is pierced around its fringes to emplace the basalts and andesites which erupt from the flanks of the volcano. It is unlikely that the "magma chamber shadow" sometimes inferred from the paucity of mafic vents in the caldera is due to a caldera-wide magma chamber such as the one proposed by *Eichelberger* [1981]. Such a chamber should be detectable by this and other experiments and has not been observed. Instead we suggest that the presence of the intrusive complex at the top of the 5.7-km/s layer implies that magmas are minimally buoyant in the upper 1–2 km of the crust and that the added elevation of the shield itself discourages eruption of denser magmas near the summit. The "shadow" then may be just a least energy gravitational phenomenon except, possibly, in the eastern caldera where the magma chamber inferred from the present study may exclude denser magmas.

The low-velocity low-Q caldera feature in layer 3 is shown as a small stratified magma chamber (Figure 14). The fractionation discussed by *Grove and Donnelly-Nolan* [1986] probably occurs or at least culminates in this chamber, resulting in the stratification. Magmas erupted from this chamber may preferentially travel laterally in the dike and intrusion complex until a path of opportunity is encountered. The vent alignments on both sides of the caldera strongly suggest that the most common ascent path is along existing normal faults such as the Gillem fault and perhaps the Vulcan lineament. Direct ascent also may occur, as Figure 14 schematically suggests for the Medicine dacite flow of *Anderson* [1941].

If magmas are tapped subhorizontally from the chamber into the dike and intrusion complex, then the reverse zonation seen in the Glass Mountain flow (dacite erupting before rhyolite) is readily explained by first drawing relatively low-viscosity dacite from the center of the chamber and later tapping rhyolite from the top of the chamber. The magma overturn mechanism proposed by *Eichelberger* [1981] is unnecessary, though it still may occur.

Whether or not the interpretive model is accepted, we can make a few direct inferences from the velocity and attenuation results.

1. The structure of Medicine Lake volcano evidently is extremely complex. This complexity is evident even though the techniques used cannot differentiate very small units or units of similar physical properties. The complexity of the geology and structure mapped at the surface continues to depth.

2. The gross structure of Medicine Lake volcano is similar to the structure at Newberry volcano in central Oregon. Both have caldera low-velocity anomalies which may be small

magma chambers, both have shallow high-velocity features roughly coincident with their calderas, and both have low-velocity flank anomalies probably reflecting a greater proportion of extrusive and sedimentary rocks there. Attenuation data are not available for Newberry volcano.

3. The presence of exactly one caldera low-velocity anomaly at each volcano and the similar depth, volume, and magnitude of velocity perturbation of these features suggest that a single relatively long-lived magma chamber is present beneath each volcano. If small chambers come and go repeatedly, the odds of having exactly one present now at a volcano are slight, and the odds of a simultaneous coincidence at both volcanoes are even less. Barring some coupling mechanism between the two volcanoes, the observed coincidence implies that each magma chamber persists for a significant fraction of the volcano's history and probably that there is only one such chamber during most of this time.

4. Finally, the high-velocity caldera anomalies are significantly different from one another in detail. This feature at Newberry volcano is a ring or cylinder structure underlying well-mapped caldera ring faults. It is thought to be cone sheets intruding these faults and partly controlling hydrothermal circulation in about the upper 1 km of the volcano [*Stauber et al.*, 1985; *Sammel et al.*, 1988]. At Medicine Lake volcano, the same structure gives no hint of a ring shape and underlies a much less pronounced caldera. This difference well may affect shallow hydrothermal circulation at the two volcanoes and explain why Medicine Lake volcano has only one mapped fumarole, while Newberry volcano has two extended thermal spring areas plus one weak fumarole area. The limited development of hydrothermal activity at both volcanoes compared, for example, to the Lassen Peak area, probably is due to substantial infiltration of meteoric water at the summits [*Sammel et al.*, 1988].

CONCLUSIONS

The NeHT seismic tomography method has been applied successfully to Medicine Lake volcano to give both velocity and attenuation images of the upper crust. Ray path and artifact uncertainties exist for the caldera low-velocity feature in layer 3 but are mitigated by a shallow structure stripping method and by direct observation of the feature in δt^* data. We believe that a low-velocity low-Q region exists beneath the eastern caldera in layer 3 and interpret this feature as the magma chamber feeding several of the youngest summit silicic eruptions. The chamber volume does not exceed a few tens of cubic kilometers.

Shallower structures are imaged with greater certainty and include the caldera high-velocity feature in layer 2 and the east flank low-velocity low-Q regions. These features lead to structural interpretations suggesting a complex eruption path for the summit silicic flows and supporting a major east-down normal fault beneath Glass Mountain. Finally, a region of high Q but normal velocity beneath Mount Hoffman may be a low-porosity, possibly hot, subsolidus intrusion. A high-velocity low-Q region beneath the eastern caldera may contain boiling water.

Acknowledgments. We wish to thank Julie Donnelly-Nolan, Chris Sanders, Gene Humphreys, Rick Aster, Paul Kasameyer, Al Duba, and Norm Burkhard for their reviews of the manuscript. Suggestions by Doug Stauber, Bill Ellsworth, and Steve Taylor significantly improved the work, and Mark Mathews discovered the errors in equation (13). We gratefully acknowledge the assistance of the 33-person U.S. Geological Survey field crew listed by Berge et al. (1986) and the seven-person Lawrence Livermore National Laboratory field crew (Cal Broadwater, Norm Burr, Terry Hauk, Don Rock, Don Trimmer, Don Watwood, and Larry Weathem), without whose energetic assistance this complex experiment could not have been performed. The modified ACH routine was written originally by David Oppenheimer based on the code by Bill Ellsworth and George Zandt. This work was supported by the U.S. Geological Survey's Geothermal Research Program and the Department of Energy's Geothermal and Hydropower Technology Division.

REFERENCES

Achauer, U., L. Greene, J. R. Evans, and H. M. Iyer, Nature of the magma chamber underlying the Mono Craters area, eastern California, as determined from teleseismic travel time residuals, *J. Geophys. Res.*, *91*, 13,873–13,891, 1986.

Aki, K., A. Christoffersson, and E. S. Husebye, Determination of the three-dimensional seismic structure of the lithosphere, *J. Geophys. Res.*, *82*, 277–296, 1977.

Anderson, C. A., Volcanoes of the Medicine Lake highland, California, *Univ. Calif. Berkeley Publ. Geol. Sci.*, *25*, 347–421, 1941.

Berge, P. A., J. R. Evans, J. J. Zucca, W. M. Kohler, W. D. Mooney, P. B. Dawson, and M. H. Smith, High-resolution seismic investigation of the Medicine Lake volcano, California, *U.S. Geol. Surv. Open File Rep.*, *86-362*, 101 pp., 1986.

Ciancanelli, E. V., Geology of Medicine Lake volcano, California, *Trans. Geotherm. Resour. Counc.*, *7*, 135–140, 1983.

Donnelly-Nolan, J., Structural trends and geothermal potential at Medicine Lake volcano, northeastern California (abstract), *Eos, Trans. AGU*, *64*, 898, 1983.

Donnelly-Nolan, J. M., Geothermal potential of Medicine Lake volcano, in *Proceedings of the Workshop on Geothermal Resources of the Cascade Range*, edited by M. Guffanti and L. J. P. Muffler, *U.S. Geol. Surv. Open File Rep.*, *85-521*, 34–36, 1985.

Donnelly-Nolan, J. M., Medicine Lake volcano, California, and its geothermal potential, *U.S. Geol. Surv. Circ.*, *974*, 12–13, 1986.

Donnelly-Nolan, J. M., Dike complex under Medicine Lake volcano, northern California Cascades, in *Abstract Volume: Hawaii Symposium on How Volcanoes Work*, p. 57, Hawaiian Volcano Observatory, Hilo, Hawaii, 1987.

Donnelly-Nolan, J. M., A magmatic model of Medicine Lake volcano, California, *J. Geophys. Res.*, *93*, 4412–4420, 1988.

Draper, N. R., and H. Smith, *Applied Regression Analysis*, 407 pp., John Wiley, New York, 1966.

Eichelberger, J. C., Mechanism of magma mixing at Glass Mountain, Medicine Lake highland volcano, California, *U.S. Geol. Surv. Circ.*, *838*, 183–189, 1981.

Ellsworth, W. L., Three-dimensional structure of the crust and mantle beneath the island of Hawaii, Ph.D. thesis, 237 pp., Mass. Inst. of Technol., Cambridge, 1977.

Evans, J. R., Compressional-wave velocity structure of the Medicine Lake volcano and vicinity from teleseismic relative traveltime residuals (extended abstract), *Tech. Prog. Abs. and Biog., 52nd Annual Meeting*, pp. 482–485, Soc. Explor. Geophys., Tulsa, OK, 1982*a*.

Evans, J. R., Running median filters and a general despiker, *Bull. Seismol. Soc. Am.*, *72*, 331–338, 1982*b*.

Finn, C., and D. L. Williams, Gravity evidence for a shallow intrusion under Medicine Lake volcano, California, *Geology*, *10*, 503–507, 1982.

Fisher, J. R., The volumetric properties of H_2O—A graphical portrayal, *J. Res. U.S. Geol. Surv.*, *4*, 189–193, 1976.

Grove, T. L., and J. M. Donnelly-Nolan, The evolution of young silicic lavas at Medicine Lake volcano, California: Implications for the origin of compositional gaps in calc-alkaline series lavas, *Contrib. Mineral. Petrol.*, *92*, 281–302, 1986.

Him, A., and A. Nercessian, Mont Dore: Etude structurale tridimensionnelle par des methodes des sismique transmission, *Rep. on Contract 578 78 EGF*, 118 pp., R and D Program Geotherm. Energy, Comm. of the Eur. Communities, Brussels, 1980.

Ito, H., J. DeVilbiss, and A. Nur, Compressional and shear waves in saturated rock during water-steam transition, *J. Geophys. Res.*, *84*, 4731–4735, 1979.

Iyer, H. M., J. R. Evans, G. Zandt, R. M. Stewart, J. M. Coakley, and J. N. Roloff, A deep low-velocity body under the Yellowstone caldera, Wyoming: delineation using teleseismic *P* wave residuals and tectonic interpretation, *Geol. Soc. Am. Bull., Part I*, *92*, 792–798, 1981*a*.

Iyer, H. M., J. R. Evans, G. Zandt, R. M. Stewart, J. M. Coakley, and J. N. Roloff, A deep low-velocity body under the Yellowstone caldera, Wyoming: delineation using teleseismic *P* wave residuals and tectonic interpretation, *Geol. Soc. Am. Bull., Part II*, *92*, 1471–1646, 1981*b*.

King, P. B., Tectonic map of North America, scale 1:5,000,000, U.S. Geol. Surv., Menlo Park, Calif., 1969.

Kissling, E., W. L. Ellsworth, and R. S. Cockerham, Three-dimensional structure of the Long Valley caldera, California, region by geotomography, *U.S. Geol. Surv. Open File Rep.*, *84-939*, 188–220, 1984.

MacLeod, N. S., D. R. Sherrod, and L. A. Chitwood, Geologic map of Newberry volcano, Deschutes, Klamath, and Lake counties, Oregon, scale 1:62,500, *U.S. Geol. Surv. Open File Rep.*, *82-847*, 27 pp. and 1 plate, 1982.

Mavko, G. M., Velocity and attenuation in partially melted rocks, *J. Geophys. Res.*, *85*, 5173–5189, 1980.

Nercessian, A., and A. Hirn, Identification of 3-D bodies by Moho reflected waves: Application to the Mont Dore area, in *Advances in European Geothermal Research*, pp. 622–631, D. Reidel, Hingham, Mass., 1980.

Nercessian, A., A. Hirn, and A. Tarantola, Three-dimensional seismic transmission prospecting of the Mont Dore volcano, France, *Geophys. J. R. Astron. Soc.*, *76*, 307–315, 1984.

Richards, P. G., and W. Menke, The apparent attenuation of a scattering medium, *Bull. Seismol. Soc. Am.*, *73*, 1005–1022, 1983.

Saltzman, N., J. A. Rial, and J. J. Zucca, Modeling near surface structure at Medicine Lake volcano, CA, using *P* wave polarizations (abstract), *Eos, Trans. AGU*, *68*, 351, 1987.

Sammel, E. A., S. E. Ingebritsen, and R. H. Mariner, The hydrothermal system at Newberry volcano, Oregon, *J. Geophys. Res.*, *93*, 10,149–10,162, 1988.

Solomon, S. C., and M. N. Toksoz, Lateral variation of attenuation of *P* and *S* waves beneath the United States, *Bull. Seismol. Soc. Am.*, *60*, 819–838, 1970.

Stauber, D. A., S. M. Green, and H. M. Iyer, Three-dimensional [illegible] velocity structure of the crust below Newberry volcano, Oregon, *J. Geophys. Res.*, *93*, 10,095–10,107, 1988.

Stauber, D. A., H. M. Iyer, W. D. Mooney, and P. B. Dawson, Three-dimensional *P* velocity structure of the summit caldera of Newberry volcano, Oregon, *Trans. Geotherm. Resour. Counc., Part II*, 411–415, 1985.

Taylor, S. R., B. B. Bonner, and G. Zandt, Attenuation and scattering of broadband *P* and *S* waves across North America, *J. Geophys. Res.*, *91*, 7309–7325, 1986.

Teng, T.-L., Attenuation of body waves and the *Q* structure of the mantle, *J. Geophys. Res.*, *73*, 2195–2208, 1968.

Ward, R. W., and C.-Y. Young, Mapping seismic attenuation within geothermal systems using teleseisms with application to The Geysers-Clear Lake region, *J. Geophys. Res.*, *85*, 5227–5236, 1980.

Young, C.-Y., and R. W. Ward, Three-dimensional Q^{-1} model of the Coso Hot Springs Known Geothermal Resource Area, *J. Geophys. Res.*, *85*, 2459–2470, 1980.

Young, C.-Y., and R. W. Ward, Attenuation of teleseismic *P* waves in The Geysers-Clear Lake region, *U.S. Geol. Surv. Prof. Pap.*, *1141*, 149–160, 1981.

Zucca, J. J., G. S. Fuis, B. Milkereit, W. D. Mooney, and R. D. Catchings, Crustal structure of northeastern California, *J. Geophys. Res.*, *91*, 7359–7382, 1986.

J. R. Evans, U.S. Geological Survey, MS 977, 345 Middlefield Road, Menlo Park, CA 94025.

J. J. Zucca, Lawrence Livermore National Laboratory, MS L-205, P.O. Box 808, Livermore, CA 94550.

(Received February 2, 1988;
revised July 5, 1988;
accepted July 19, 1988.)